



1 **Trends in measured and modeled lower stratospheric Antarctic vortex ozone**
2 **over the past two decades**

3 Lucien Froidevaux¹, Michael J. Schwartz², Douglas E. Kinnison³, Nathaniel J. Livesey²,
4 Gloria L. Manney⁴, Michelle L. Santee², William G. Read², and Ryan A. Fuller²

5

6 ¹Retired

7 ²Jet Propulsion Laboratory, California Institute of Technology, Pasadena, California, USA

8 ³NSF National Center for Atmospheric Research (NSF NCAR), Boulder, Colorado, USA

9 ⁴NorthWest Research Associates, New Mexico Institute of Mining and Technology, Socorro, New
10 Mexico, USA

11 *Correspondence to:* Michael.J.Schwartz@jpl.nasa.gov

12 **Abstract.** We analyze 2004 to 2023 winter/spring lower stratospheric Antarctic ozone data from
13 the Aura Microwave Limb Sounder (MLS), along with similarly sampled profiles from two
14 simulations from the Whole Atmosphere Community Climate Model (WACCM) run with
15 specified dynamics. One of these simulations uses fixed surface organic halogens from 1998
16 onward. The interannual variability in MLS vortex-average ozone is well matched by WACCM,
17 although WACCM shows a slightly smaller seasonal decrease. Probability density functions of
18 vortex ozone profiles reveal slow increases in the smallest values; WACCM shows good
19 agreement with MLS distribution shifts and simple linear trends. We also use multivariate linear
20 regression with two periodic functions and a proxy for polar stratospheric clouds to derive trends
21 in vortex-average ozone during September and October. Calculated trends are consistent with slow
22 Antarctic vortex ozone recovery from the impact of ozone-depleting substances, with values
23 between ~ 5 and 16 ppbv yr⁻¹ in the 56–100 hPa layer. WACCM results agree well with those from
24 MLS. The simulation with fixed surface organic halogens is consistent with zero trend. We also
25 apply the Match technique, which follows MLS-observed parcels along trajectories to estimate
26 vortex-average chemical ozone loss. Match estimates also show slow reductions in seasonal



27 Antarctic ozone loss, although few of the Match results represent greater than two-sigma
28 departures from zero. Our work confirms the emergence of ozone recovery, a key goal of the Aura
29 mission, and underscores the importance of the 1987 Montreal Protocol and its Amendments in
30 curtailing emissions of ozone-depleting substances.

31 © 2026 California Institute of Technology. Government sponsorship acknowledged.

32 **1 Introduction**

33 Early warnings were made in the 1970s (Molina and Rowland, 1974) regarding threats to the
34 Earth's stratospheric ozone (O_3) layer from the decomposition of chlorofluorocarbons (CFCs)
35 emitted at the surface by industrial activities. There were human health implications from
36 increased ultraviolet (UV) radiation at the surface, which would arise from a reduction in UV
37 absorption by stratospheric ozone. The subsequent discovery (Farman et al., 1985) of the recurring
38 winter/spring ozone hole development over Antarctica has made polar ozone the subject of
39 particularly intense studies. The 1987 Montreal Protocol and its subsequent Amendments curtailed
40 the surface emissions of ozone-depleting substances (ODSs). The following decades saw a large
41 increase in the database of polar (and global) ozone observations, as well as in the understanding
42 of the main causes of this phenomenon and its evolution (e.g., Solomon, 1999; Chipperfield,
43 Santee, et al., 2022). In the polar regions, lower stratospheric ozone is destroyed during the cold
44 winter and spring after the release of active chlorine from its stratospheric reservoir species (mainly
45 HCl and ClONO₂), via heterogeneous chemical reactions enabled on the surfaces of polar
46 stratospheric clouds (PSCs); chlorine and bromine species both contribute to the ozone destruction
47 that peaks in September and October, after the return of sunlight to the polar regions.



48 As mentioned in recent Ozone Assessment Reports (WMO, 2018; WMO, 2022), a consensus
49 has been building that, after a significant slowdown in global decreases of lower stratospheric and
50 total column ozone abundances, we are now in the phase of ozone recovery from the effects of
51 ODSs. The post-2000 period has been characterized by a slow decline in equivalent effective
52 stratospheric chlorine (EESC), a metric used to represent the combined impact of total
53 stratospheric chlorine and bromine abundances (Newman et al., 2007; Engel et al., 2018). EESC
54 is related, in turn, to ODS emission changes at the surface; Lickley et al. (2024) have recently
55 assessed how and why the estimates of EESC and global ozone recovery dates have slowly evolved
56 over the past two decades. There has been slowly growing evidence for the emergence of lower
57 stratospheric Antarctic ozone healing, although lower stratospheric ozone trends are hard to detect
58 at other latitudes, including in the Arctic region, where larger dynamical variability occurs. Signs
59 of the emergence of Antarctic ozone recovery since about the turn of the 21st century, following
60 global decreases in ODSs, have been reported in analyses of a variety of data sets, including in situ
61 data, satellite-based profiles and column ozone, coupled with model or data assimilation studies
62 (e.g., Solomon et al., 2016; de Laat et al., 2017; Weber et al., 2018; Strahan et al., 2018; Pazmiño
63 et al., 2018; WMO, 2022). Antarctic ozone profiles from ozonesondes and satellites showed that
64 very small ozone abundances occurred seasonally after 1987, with destruction processes
65 “saturating,” that is, insensitive to further increases in ODSs because there was no more ozone to
66 destroy. Occurrences of near-zero ozone reached a maximum at the turn of the century, after which
67 there were decreases in the saturation of ozone loss (Kuttippurath et al., 2018; Chipperfield,
68 Santee, et al., 2022). Quoting the WMO (2022) Assessment, new results since 2018 support the
69 findings that “the Antarctic ozone hole has generally diminished in size and depth since the year
70 2000.” More recent work by Pazmiño et al. (2023) employs a model-based passive ozone tracer



71 and total ozone column observations since 1989 to analyze Antarctic ozone recovery based on
72 three different metrics: maximum ozone loss at the end of winter, the onset dates for ozone loss,
73 and a residual method that is coupled to regression analyses tied to the volume of PSCs (VPSC).
74 Their study confirms the ozone recovery in the Antarctic, despite the increased interannual
75 variability in the last decade compared to earlier periods. Also, according to Strahan et al. (2018),
76 mid-September is when stratospheric ozone over Antarctica shows the largest sensitivity to
77 decreasing ODSs and when Antarctic ozone recovery rates are strongest and most easily detected.
78 The rate of decrease in Antarctic ozone is steepest in September; in October, there are more
79 dynamically induced perturbations to the vortex, before its eventual breakup, typically in
80 November or December.

81 For this work, we rely upon two decades of ozone profiles retrieved from Aura Microwave
82 Limb Sounder (MLS) measurements inside the Antarctic vortex, as detailed in Section 2.
83 Measurements of global ozone as well as the variability in temperature and chemical processing
84 inside the Arctic and Antarctic stratospheric vortices have been obtained nearly continuously by
85 MLS since the Aura launch in July 2004 (e.g., Santee et al., 2005, 2011, 2024; Manney et al., 2011,
86 2023; Kuttippurath et al., 2015). By using this unique, continuous, well-sampled and stable ozone
87 dataset, having the same regular data coverage over time, we avoid potential trend uncertainties
88 that could arise from a merged record combining multiple datasets obtained using different
89 measurement techniques with different spatio-temporal coverage within the analysis period. We
90 compare the MLS data to results from two simulations from the Whole Atmosphere Chemistry
91 Climate Model (WACCM), both using specified dynamics, but one of them having surface ODSs
92 fixed at 1998 levels; after 4–5 years, the fixed-ODS conditions lead to nearly invariant EESC levels
93 in the polar stratosphere. In Section 3, we analyze Antarctic ozone distributions from MLS and the



94 WACCM simulations, with a focus on Probability Density Functions (PDFs) and simple linear
95 trends. In addition, we comment briefly on the observed and modeled HCl and HNO₃ distributions
96 inside the Antarctic vortex. Trends in September and October vortex-average ozone profiles are
97 then quantified using Multivariate Linear Regression (MLR), to obtain better fits to the time series
98 and reduce the resulting trend uncertainties. We also discuss another metric, namely trends in
99 Antarctic ozone loss over the period from 2005 to 2023 computed using the Match technique,
100 which follows a multitude of air parcels inside the winter/spring lower stratospheric Antarctic
101 vortex to diagnose chemical ozone loss (Livesey et al., 2015). We provide some discussion and
102 conclusions in Section 4.

103 **2 Description of datasets and model simulations**

104 **2.1 MLS data**

105 The observations of stratospheric ozone by Aura MLS provide the backbone for this work. Aura
106 is in a near-polar sun-synchronous orbit, and the MLS antenna scans the atmosphere vertically in
107 front of the spacecraft from the surface to ~90 km every 24.7 s. MLS obtains atmospheric
108 composition profiles of various species, along with temperature and cloud ice profiles, based on
109 day and night thermal emission measurements near 118, 190, 240, and 640 GHz, and (for parts of
110 the mission) near 2.5 THz. Waters et al. (2006) describe the MLS measurement technique. Read
111 et al. (2006) provide information regarding the simulated MLS forward model and related spectra.
112 The MLS Level 2 retrievals (Livesey et al., 2006) use the optimal estimation approach (Rodgers,
113 2000); there is no assumption of atmospheric homogeneity along the line of sight (see Livesey and
114 Read, 2000). These retrievals provide nearly 3500 daily profiles for temperature and for each
115 species, day and night, from 82°S to 82°N, with regular temporal and spatial sampling. The MLS



116 data used here are from the version 5 software (Livesey et al., 2022); the standard ozone product
117 is retrieved from the MLS measurements near 240 GHz. Specifics of MLS data characterization
118 and data quality, along with estimated errors and related information, are described by Livesey et
119 al. (2022). We follow all the standard recommendations for data screening. The vertical resolution
120 for ozone profiles is about 2.7 km in the vertical range considered here. Typical single-profile
121 precision estimates for ozone, based on MLS radiance noise, range from 0.02 ppmv in the
122 lowermost stratosphere to 0.2 ppmv at 1 hPa. Estimates of systematic errors were obtained by
123 modeling the impact of individual error sources (e.g., calibration and spectroscopic uncertainties)
124 on the MLS ozone profiles; an accuracy of 5–10% can be expected in the lower stratosphere,
125 consistent with the typical agreement between MLS ozone and correlative datasets (e.g.,
126 Froidevaux et al., 2008; Jiang et al., 2007; Livesey et al., 2008). Comparisons of various satellite
127 and ground-based ozone measurements by Hubert et al. (2016) have demonstrated that the MLS
128 capability for detection of vertically resolved ozone trends is among the best in terms of both
129 stability and daily coverage. Furthermore, differences between stratospheric ozone columns from
130 MLS and the Aura Ozone Monitoring Instrument (OMI) show no significant drift (Ziemke et al.,
131 2019).

132 **2.2 Model simulations**

133 For comparison with 20 years of MLS Antarctic polar vortex winter/spring lower stratospheric
134 observations, we have sampled two runs of the Whole Atmosphere Community Climate Model
135 version 6 (WACCM6) at MLS observation times and locations. The second simulation differs from
136 the first only by using fixed surface organic halogens at 1998 levels, which leads to stable EESC
137 values within ~4–5 years in the polar stratosphere. In this work, these runs will be denoted as
138 WACCM and WACCM-fix-EESC (or WACCM-fix, for short, in the figures), respectively.



139 WACCM6 is a component of the Community Earth System Model (CESM) version 2.2
140 (Gettelman et al., 2019; Danabasoglu et al., 2020). WACCM6 uses a “high-top” set of 70 model
141 levels between the surface and the lower thermosphere (~140 km). The model has a horizontal
142 resolution of 0.95° latitude \times 1.25° longitude. WACCM6 includes representations of boundary
143 layer processes, shallow convection, liquid cloud macrophysics, and cloud microphysics. The
144 chemical scheme includes the O_x , NO_x , HO_x , ClO_x , and BrO_x families, along with CH_4 and its
145 degradation products, as well as primary non-methane hydrocarbons and related oxygenated
146 organic compounds (Emmons et al., 2020). Reaction rates follow the JPL Publication 19-5
147 recommendation (Burkholder et al., 2019). The chemical scheme includes a total of 231 species
148 and 583 chemical reactions broken down into 150 photolysis reactions, 403 gas-phase reactions,
149 13 tropospheric, and 17 stratospheric heterogeneous reactions. The photolytic reactions are based
150 on both inline chemical modules and a lookup table approach (Kinnison et al., 2007).

151 To accurately represent polar stratospheric temperature and winds, the simulations are run in
152 the ‘specified dynamics’ (SD) mode. The model dynamical constraints are taken from
153 meteorological fields provided by the Modern-Era Retrospective Analysis for Research and
154 Applications version 2 (MERRA-2; Gelaro et al., 2017). The MERRA-2 fields, i.e., zonal and
155 meridional winds and temperature, are first regrided to the model horizontal and vertical grids.
156 The model nudging (Davis et al., 2022) is updated at every (30 min) time step using the closest 3-
157 hourly MERRA-2 fields; nudging timescales are set at 12 hours for WACCM6. Both model
158 simulations in this study use identical MERRA-2 meteorological fields and subsequently represent
159 identical dynamical variability. The 11-year solar cycle variability is taken from the Naval
160 Research Laboratory’s (NRL) Solar Spectral Irradiance model, version 2 (NRLSSI2; Coddington
161 et al., 2016). WACCM6 incorporates geomagnetic variability that affects the flux of energetic



162 particles precipitating into the atmosphere, ionizing or dissociating major species. Ion-pair
163 production rates (IPR) by galactic cosmic rays, solar protons, and medium-energy electrons are
164 also prescribed, following Matthes et al. (2017). The IPR rates are converted into rates of
165 production for odd-hydrogen and odd-nitrogen species following Jackman et al. (2009). Volcanic
166 SO₂ emissions (used in sulfate aerosol density calculations) are derived for significant volcanic
167 eruptions using the Neely and Schmidt (2016) database updated through the year 2022. The model
168 scenario used here is based on historical forcings (and recent updates) from the Climate Model
169 Intercomparison Project – Phase 6 (CMIP6; Meinshausen et al., 2017). The forcings include
170 greenhouse gases (CH₄, N₂O, and CO₂) and organic halogens. After 2014, the greenhouse gas and
171 organic halogen inputs follow the CMIP6 SSP5-8.5 scenario that projects inputs beyond 2014
172 (O’Neill et al., 2016; Riahi et al., 2017; Meinshausen et al., 2020).

173 The polar heterogeneous chemistry module that is important for this work is discussed in
174 Wegner et al. (2013), Solomon et al. (2015), Wilka et al. (2021), and Weimer et al. (2023). The
175 Wegner et al. study used Aura MLS observations of Antarctic HNO₃ and H₂O and PSC
176 distributions from the Cloud-Aerosol Lidar with Orthogonal Polarization (CALIOP) on the Cloud-
177 Aerosol Lidar and Infrared Pathfinder Satellite Observation (CALIPSO) satellite. The CALIOP
178 observations showed that in both polar regions, PSCs throughout the entire winter are mainly a
179 mixture of nitric acid trihydrate (NAT) particles and supercooled ternary solution (STS) droplets.
180 Typical WACCM assumptions about PSC formation at a given NAT supersaturation did not
181 produce such a population of mixed particles and led to earlier removal of HNO₃ from the gas
182 phase compared to Aura MLS observations. Wegner et al. (2013) updated the model’s polar
183 stratospheric chemistry scheme, allowing only a fraction of the total available HNO₃ to freeze to
184 NAT, with the remaining HNO₃ forming STS, forcing the formation of mixed PSCs in the model.



185 With this approach, both NAT and STS were present throughout the model polar winter, and the
186 observed gas-phase polar HNO₃ abundance was better represented. Solomon et al. (2015) found
187 that the updated heterogeneous chemistry approach recommended by Wegner et al. (2013) is
188 strongly temperature dependent, where a degree or two difference can cause large changes in
189 chemical reactivity and PSC surface area densities. Therefore, it is necessary to run WACCM6 in
190 specified dynamics mode when comparing with observed ozone depletion.

191 PSCs not only activate chlorine through heterogeneous chemical processing but also denitrify
192 the atmosphere through removal of HNO₃ from the gas phase and subsequent sedimentation (e.g.,
193 Solomon, 1999). Removing HNO₃ reduces the abundance of NO₂, which, in turn, enhances active
194 chlorine (ClO) by reducing ClONO₂ formation rates, thus affecting ozone destruction. Initial
195 comparisons of simulated ozone profiles to both ozonesondes and MLS showed that the model's
196 standard approach with a NAT number density (N_{NAT}) of 0.01 cm⁻³ (Wegner et al., 2013) was not
197 denitrifying enough. A lower N_{NAT} corresponds to larger individual particles and leads to more
198 denitrification by increasing the particles' settling velocities. Wilka et al. (2021) found that
199 adopting a value of N_{NAT} of $\sim 10^{-5}$ cm⁻³ resulted in the closest match to observed ozone profiles
200 over a wide vertical range and also matched the MLS HNO₃ abundances better than other values.
201 A more detailed analysis of the choice of N_{NAT} was conducted by Weimer et al. (2023). That study
202 compared PDFs of modeled ClONO₂, ozone, and HNO₃ within the polar vortex with data from the
203 Michelson Interferometer for Passive Atmospheric Sounding onboard the Environmental Satellite
204 (MIPAS/Envisat), which operated between 2002 and 2012. Weimer et al. used the maximum
205 difference between the WACCM and MIPAS cumulative density functions to check whether the
206 distributions were distinguishable in a statistical sense. To identify the impact of NAT on the
207 distributions of the above-mentioned species, Weimer et al. (2023) performed sensitivity



208 simulations varying N_{NAT} between 10^{-2} and 10^{-5} cm^{-3} and concluded that a value of N_{NAT} equal to
209 5×10^{-4} cm^{-3} best represented the denitrification parameterization for WACCM. This value is used
210 in the present study.

211 **3 Analyses and results**

212 **3.1 Antarctic ozone changes and related Probability Density Functions**

213 The Antarctic vortex edge is defined using a height-dependent threshold of scaled potential
214 vorticity, based on the work by Lawrence et al. (2018). Figure 1 shows, for each year of MLS data
215 from 2005 to 2024, time series from austral early winter through spring of weekly vortex-average
216 differences from each year's respective July 1-10 baseline; only a minor amount of ozone loss
217 generally occurs before July, as evidenced by the grey shades in June and July. In Figure 2, we
218 show the same vortex-average changes over the winter/spring for the (standard) WACCM
219 simulation used in this work. The MLS data show that several years (2006, 2008, 2014, 2020,
220 2021, 2023, and 2024) have lower average values in October, after most of the chemical loss has
221 occurred, especially in the lower portion of the vortex. Although WACCM generally shows
222 slightly smaller ozone changes from baseline than MLS in September and October, the measured
223 and modeled patterns of interannual variability are similar. The correlation between ozone losses
224 and minimum temperatures in the lower stratospheric Antarctic vortex has been noted before (e.g.,
225 Kuttippurath et al., 2015; Roy et al., 2024). We discuss the correlation between temperature and
226 ozone in the Antarctic vortex further below in the context of MLR fits to the MLS vortex-average
227 ozone time series from 2005 to 2023.

228 Figure 3(a) shows the climatological distribution of weekly average MLS ozone values from
229 early-June to late-November for the period 2005–2023, and the difference between WACCM and



230 MLS results is seen in Fig. 3(b). The largest decreases in lower stratospheric Antarctic ozone occur
231 during August and September (e.g., Chipperfield, Santee, et al., 2022; Strahan and Douglass, 2018;
232 Santee et al., 2024). Indeed, Fig. 3(a) shows that changes in MLS ozone occur mostly at pressures
233 larger than 20 hPa after early to mid-August, with effects of downward transport visible in the
234 contours at smaller pressures. The upper region is where the WACCM values are smaller than the
235 MLS abundances, possibly because downward transport velocities are too small in the model;
236 some of the absolute differences may also come from systematic errors in the MLS data, since
237 systematic uncertainties are as large as 5–15% (Livesey et al., 2022). In the main region of
238 chemical destruction after early September, the WACCM values tend to be larger than MLS data
239 by about 100 ppbv, or ~25% (Fig. 3(b)). Fig. 3(c) shows that WACCM O₃ mixing ratios at 68 hPa
240 are ~300 ppbv lower than those observed by MLS in June and July but end up on the higher end
241 in October, implying somewhat smaller modeled seasonal ozone loss than is observed; a
242 systematic bias between modeled and measured ozone would not produce this different behavior
243 in the slope of the ozone change.

244 Fig. 3(d) shows the slopes of linear fits to the time series of vortex-average ozone from MLS
245 and both WACCM simulations at 68 hPa for 2004 to 2023. The trend estimates track well between
246 MLS and WACCM, with positive trends typically between about 5 and 16 ppbv yr⁻¹, depending
247 upon the date (weekly average) in winter or spring; the trends from MLS and WACCM both peak
248 in mid-September. However, the trends obtained from the WACCM-fix-EESC simulation are
249 consistent with a trend value of zero, as one might expect from such a fixed-EESC scenario. The
250 seasonal patterns of changes in WACCM and MLS-derived trends are generally consistent
251 throughout the winter/spring season from 147–14.7 hPa (not shown). The differences between
252 WACCM and WACCM-fix-EESC trends are largest at 68.1 hPa and lose significance in this



253 analysis by 14.7 hPa. At levels other than 68.1 hPa, there is generally more departure of the
254 WACCM-fix-EESC trends from zero, likely reflecting the impact of changes in dynamics that are
255 generally consistent among WACCM, WACCM-fix-EESC and MLS. More sophisticated ozone
256 trend analyses are pursued in Sect. 3.2.

257 Figure 4 depicts PDFs for vortex-average ozone (panels a, c, and e) and related trends in these
258 distributions (panels b, d, and f) for the week centered on September 12. Panels a, c and e all have
259 sharply peaked distributions up to 83 hPa, with the broader distributions at 68–18 hPa reflecting
260 larger spatial and/or interannual variability in lower stratospheric ozone. WACCM generally has
261 slightly larger values than those of MLS at these levels. WACCM also lacks the near-zero values
262 seen in the tail of the MLS PDF at 83–26 hPa, where MLS has observed some cases of early near-
263 complete ozone depletion. At 68–46 hPa, the MLS single-observation precision is ~half of the
264 width of a 100-ppmv histogram bin, so the MLS points near zero do not merely reflect random
265 noise. The WACCM-fix-EESC distribution at these levels also has more of the lowest (100–200
266 ppbv) ozone values than the standard WACCM simulation, suggesting less recovery, as implied
267 also by Fig. 3(d); a larger value for EESC would indeed qualitatively account for such a difference
268 between the two model simulations.

269 The right side of Fig. 4 shows how the PDFs tend to change over time (from 2005 to 2023),
270 with both MLS and WACCM showing shifts in the peaks of the distributions over the 20-year
271 record, with fewer occurrences of values below 500 ppbv (green and blue areas on the left edge of
272 panels (b) and (d)) and more at 800 ppbv and higher (brown areas of panels (b) and (d)). Bins
273 without black stippling have trends with magnitudes more than twice the uncertainty in the fitted
274 values. PDF trends for WACCM-fix-EESC in Figure 4(f) show no shift from lower to higher
275 values at 68-18 hPa, but rather an apparent tightening of the PDF, with brown sandwiched between



276 green where panels (b) and (d) show such a shift. Figure 5 helps to visualize this shift by comparing
277 the MLS PDFs at 38 and 82 hPa for a week in mid-September in two five-year periods at the
278 beginning (2004–2008, in blue) and end (2019–2023, in red) of the study period; in the later years,
279 the peak of the distributions has clearly shifted towards larger abundances, and there are almost no
280 ozone values below 500 ppbv. This result is consistent with work by Kuttippurath et al. (2018),
281 who demonstrated decreasing saturation in lower stratospheric Antarctic ozone loss. However, if
282 we consider a week in mid-October, results show only subtle changes in the MLS PDF trends (Fig.
283 S1); the ozone values are too small (and perturbed) during this period to allow for a robust trend
284 detection.

285 Figure 6 shows MLS HCl in the same format as for O₃ in Fig. 3. MLS shows highly depleted
286 climatological HCl abundances during winter for pressures larger than 20 hPa, with a sharp
287 increase at the end of September towards values between 2.5 and 3 ppbv in the spring (Fig. 6(a)).
288 The differences in Fig. 6(b) indicate that WACCM has HCl values that are slightly larger in the
289 winter but recover in the spring to mean values that are slightly smaller than those observed by
290 MLS, as shown also at 68 hPa in Fig. 6(c), where modeled HCl does not quite reach 2.5 ppbv at
291 the end of November. The Antarctic early-winter discrepancy between HCl rates of decrease from
292 models and from MLS has been addressed recently by Grooss et al. (2025), who point out that
293 additional chemical mechanisms involving Cl₂O₂, HOCl, and HOCl could resolve this issue,
294 although there is a need for more laboratory validation regarding the reaction rates of these
295 postulated mechanisms. The fact that WACCM has somewhat less HCl in the polar spring may in
296 part reflect a total inorganic chlorine (Cly) value that is slightly low, possibly because of a deficit
297 in very short-lived substances (VSLs) and some inaccuracies in repartitioning during chlorine
298 deactivation. Fig. 6(d) shows linear trends of about -0.02 ppbv yr⁻¹ for vortex-average MLS HCl



299 in late spring, when 68.1 hPa HCl abundances (~ 2.8 ppbv) are comparable to mid-to-upper
300 stratospheric HCl values. These trends correspond to about -0.7% yr⁻¹, which is somewhat larger
301 than global trends (since the turn of the century) in upper stratospheric HCl of about -0.3 to -0.5%
302 yr⁻¹ (WMO, 2022). In contrast, the WACCM-fix-EESC simulation leads to HCl trend results that
303 are consistent with zero trend, as one would expect.

304 Figure 7 is analogous to Figs. 3 and 6, but for modeled and observed HNO₃. Strong depletion
305 of gaseous HNO₃ is observed in the climatology from MLS (panel (a)), with the WACCM
306 simulation (panel (b)) showing slightly larger values than the MLS abundances in early winter and
307 slightly lower values in the spring. As mentioned in Sect. 2.2, this WACCM fit to Antarctic HNO₃
308 observations is clearly better than that in previous simulations from WACCM, following
309 improvements in the modeled heterogeneous chemical processing scheme. In Fig. 7(d), the MLS
310 and modeled linear trends in HNO₃ from 2005 to 2023 all agree very well, with near-zero trend
311 for most months. During June and July, a negative trend is apparent in MLS data as well as in the
312 model simulations. Investigation of the underlying cause of these apparent trends in early-winter
313 HNO₃ is beyond the scope of this study.

314 **3.2 Further analyses of trends in Antarctic vortex ozone**

315 **3.2.1 MLR analyses of vortex-average ozone trends**

316 Here, we use 7-day means of Antarctic vortex-average ozone abundances for 2005–2023 to
317 perform multivariate linear regression analyses to produce better fits to the time series and reduce
318 the error bars compared to a fit with only a linear trend term (and a constant term). We apply the
319 same analyses to both model simulations.



320 The main regression model used here has two sets of periodic functions, both described by sine
321 and cosine terms, with period 1 and period 2 representing, respectively, a short-term and a decadal-
322 type component. Our standard run has a 2.5-yr periodicity for period 1, since we observe (see
323 further below) that most Antarctic time series exhibit short-term variability. Moreover, the quasi-
324 biennial oscillation (QBO) is a well-studied phenomenon in the Earth's stratosphere (e.g., Baldwin
325 et al., 2001; Anstey et al., 2022) that can be represented by such a periodicity; there is evidence of
326 QBO influence on Antarctic temperature and inorganic chlorine (and thus ozone) over Antarctica
327 (Strahan et al., 2014; Strahan and Douglass, 2018). We should note that using a 2- or 3-yr
328 periodicity for period 1, rather than 2.5 yr, does not lead to major changes in terms of our trend
329 results, given the typical trend uncertainties. We have also varied period 2 (see further below), but
330 our standard retrieval uses a value of 11 years, which can represent solar cycle variability, even if
331 this may not be the main cause of decadal-type variability in Antarctic ozone. The other terms in
332 the MLR analysis are a constant and a linear (trend) term.

333 Also, we use a proxy term tied to the region within the vortex with temperatures allowing the
334 possible existence of polar stratospheric clouds (PSCs). The volume (VPSC) of air that is exposed
335 to temperatures below T_{NAT} , the threshold for existence of nitric acid trihydrate (NAT) PSCs, has
336 been shown to be well correlated with springtime ozone loss in the polar vortices (e.g., Rex et al.,
337 2004; Tilmes et al., 2004). Although it is known that liquid-phase particles play a large role in the
338 destruction of polar ozone, the T_{NAT} threshold is often used as a first-order estimate of the
339 conditions necessary for significant chemical ozone destruction inside the polar vortex. To
340 describe the proxy we use for the VPSC term, we show in Figure 8 the area with temperatures
341 below T_{NAT} and the area of the vortex exposed to sunlight (Lawrence et al., 2015; Lawrence et al.,
342 2018), since sunlight is required for the photochemical processes involved in Antarctic vortex



343 ozone destruction (see the review by Solomon, 1999). In Figure 8(a) and 8(d), the areas from
344 different potential temperature levels (from 330 K to 620 K) are averaged to obtain a lower
345 stratospheric layer-average area, which is akin to a summation (or volume, VPSC). The second
346 variable represents the lower stratospheric layer-average sunlit area inside the vortex, which is
347 then multiplied by VPSC. The year-to-year variability in this product (Figure 8, right-hand panels)
348 is used as a proxy term (labeled $VPSC_{sun}$ in the fitting function below) for our MLR analysis of
349 ozone vortex-average abundances. The 2019 vortex was significantly perturbed by a September
350 sudden stratospheric warming event, leading to an anomalously small Antarctic vortex and column
351 ozone destruction (e.g., Wargan et al., 2020; Roy et al., 2024). Figure 8 shows that the lower
352 stratospheric layer-average vortex area with temperatures below T_{NAT} drops much faster in 2019
353 (panel (a)) than in a representative year like 2022 (see panel (d)); this also affects the cumulative
354 layer-average diagnostic values (thick lines) in September and October, as well as the final proxy
355 values in panels (c) and (f), even if the cumulative effect is dampened compared to the daily values
356 (thin lines).

357 The MLR time series function to be fitted for coefficients a , b , c_n , d_n , and f has the following
358 form:

$$359 \quad y(t) = a + b(t - t_m) + \sum_n (c_n \sin 2\pi t/P_n + d_n \cos 2\pi t/P_n) + f VPSC_{sun}(t)$$

360 with the yearly time series values expressed by time (t); t_m refers to the series mid-point, and the
361 linear trend term is coefficient b . The sine and cosine functions provide for periodic variations
362 with periods P_n . As mentioned above, we use two periods in the MLR equation—a short-term
363 (QBO-type) period (P_1) and a longer-term (decadal-type) period (P_2); in a sensitivity study
364 discussed later, we add a term relating to the Antarctic Oscillation.



365 In Figure 9, we show examples of the variability associated with the lower stratospheric
366 $VPSC_{sun}$ proxy from 2005–2023 for the week centered on September 19, along with the vortex-
367 average ozone abundances from MLS for that week. As indicated by the values of the correlation
368 coefficient (R), there is an anti-correlation between mean ozone and the $VPSC_{sun}$ proxy; for
369 example, the 2019 vortex, with its larger-than-usual ozone values in late September, shows a
370 positive peak, whereas the proxy indicates a low value for that year. An expanded view of this
371 correlation coefficient versus pressure level for various weeks in September and October is
372 provided in Figure 10, which shows that the anti-correlation between ozone and $VPSC_{sun}$ grows
373 between early September and late October, when the cumulative impact of chemical ozone
374 destruction peaks. To first order, we expect that a polar vortex winter/spring with lower-than-
375 average temperatures will lead to more chemical processing and larger chemical ozone destruction,
376 with relatively smaller vortex-average ozone values in the spring.

377 In Figure S2, we show that use of longer periods (9 to 11 yr) for P_2 enables the MLR analysis
378 to explain a larger fraction of the variance at pressures between 56 and 100 hPa, in comparison to
379 4- to 8-yr periods; choices of 9, 10, or 11 yr do not lead to very different correlations. We have
380 chosen to use 11 yr for our standard MLR retrievals. The 11-yr solar cycle can impact ozone
381 through standard photochemistry (related to solar ultraviolet flux) or energetic particle
382 precipitation (EPP) (e.g., Gordon et al., 2021). EPP can have a direct impact on ozone in the upper
383 stratosphere and mesosphere, as well as indirect effects from downward transport of nitrogen
384 oxides to lower altitudes, although the likely long-term impact of EPP on lower stratospheric
385 Antarctic ozone is difficult to ascertain (Maliniemi et al., 2022). However, we note that the phase
386 of the solar cycle itself does not agree with the typical phase of the proxy term that we derive from
387 the MLR fits. The correlation between the 11-yr fitted component and the solar cycle variation



388 itself changes with pressure, with a range of positive, negative, or near-zero correlations;
389 elucidating a causal relationship would require modeling that is beyond the scope of this paper.
390 Transport variability is another factor that can modulate Antarctic vortex ozone abundances (e.g.,
391 Kessenich et al., 2023). More generally, there is evidence for multi-year variability and
392 hemisphere-dependent changes in HCl (Mahieu et al., 2014) and HNO₃ (Strahan et al., 2020), with
393 changes in the circulation invoked as a likely driver; these variations could also influence the
394 variability in Antarctic ozone.

395 We show in Figure S3 the same plots as in Fig. S2, but for P_1 , the 2.5-yr period we have used
396 in our standard MLR fits. As one might expect, the fraction of variance explained by the short-
397 term period does not have sensitivity to the value of P_2 . This is shown mainly to contrast the R^2
398 values from P_1 with those from P_2 . For 56 and 68 hPa, the P_2 term explains more of the variance
399 in the ozone time series, whereas the short-term period explains more of the variance at 82 and
400 100 hPa.

401 We have applied the MLR analysis described above, including the $VPSC_{sun}$ variability term, to
402 the MLS-derived Antarctic vortex-average values from different September and October weeks
403 over 2005–2023. Examples of the ozone time series and the fits are shown in Fig. 11 at 68 and
404 100 hPa for the week centered on September 19. Both the linear component (slope of the fit) and
405 the full fit to the time series are shown; as expected, much better results are obtained with the full
406 fit. Figure 12 compares the overall results at 68 hPa for the MLR-based MLS vortex-average ozone
407 trends in September and October to the trends obtained from simple linear regression. Although
408 the trends themselves do not change very much, the trend error bars are significantly reduced in
409 the MLR case (panel (a)); on average, there is a 20–25% reduction in the error bars, with a
410 reduction of ~40% at 121 hPa and ~10% at 46 hPa. In Figure 12(b) and 12(c), we also show how



411 diagnostics of the fit quality change between these two regression methods. The MLR fits, in
412 comparison to simple linear trend analysis, yield much larger correlation coefficients (0.8 to 0.95
413 rather than 0.4 to 0.5) and smaller RMS residuals (by a factor of 30–50%). Figure S4 provides the
414 same information for 100 hPa, with similarly improved results for the MLR case.

415 Figure 13 shows the MLR-based trends for 2005–2023 at 46, 68, and 100 hPa for MLS and the
416 two WACCM simulations of Antarctic vortex ozone (sampled following the MLS viewing
417 pattern). We find that some of these lower stratospheric Antarctic vortex-average ozone trends in
418 September and October are significantly different from zero (taken here to mean further from zero
419 than the 2σ error bar) for pressures larger than 50 hPa. For example, the mid-September to early
420 October MLS ozone trends (black points) are significantly different from zero at 68 and 100 hPa.
421 Typical September MLS trends are ~ 15 ppbv yr^{-1} at 68 hPa and ~ 7 ppbv yr^{-1} at 100 hPa, while
422 October trends at these two levels are mostly between zero and 10 ppbv yr^{-1} . The WACCM
423 simulation (red points) generally matches the MLS results quite well, although the error bars are
424 slightly larger. Also, as for MLS, most of the WACCM trends in October are not significantly
425 different from zero. The WACCM-fix-EESC simulation (blue points) yields lower stratospheric
426 ozone trends that are consistent with zero, as one might expect from a fixed-EESC scheme. We
427 provide in Figs. 14 and 15, respectively, the correlation coefficients and the RMS residuals, as
428 introduced in Fig. 12 for MLS, for the results from MLS, WACCM, and WACCM-fix-EESC at
429 46, 68, and 100 hPa. At 68 and 100 hPa, the R values typically lie between 0.8 and 0.95 for MLS
430 and WACCM, with slightly lower values for WACCM-fix-EESC. Correlation coefficients are
431 somewhat lower in general at 46 hPa, a region where the trends are most often found to be not
432 significant. The variation of the WACCM RMS residuals as a function of pressure follows that



433 obtained for MLS; there is not much variation in these, or in the R values, as a function of the
434 September and October dates.

435 We also provide another way of roughly estimating the changes that occur in winter/spring
436 inside the Antarctic vortex, by taking the differences (ΔO_3) between the vortex-average ozone
437 values in September or October and the mean vortex ozone values from the first week in July,
438 before substantial chemical ozone loss has occurred, especially in the lower stratosphere, where
439 the positive trends are most significant. This approach is commonly employed to partially mitigate
440 the effects on ozone arising from transport-related variability. For example, Strahan et al. (2019)
441 used this methodology and noted that the majority of ozone loss occurs after early July. Figure 16
442 gives trends in the lower stratosphere for the MLS, WACCM, and WACCM-fix-EESC cases;
443 values are close to and consistent with the results in Fig. 13, which considers the actual ozone
444 values rather than differences from an early winter baseline.

445 Figure 17 provides a summary of the MLS, WACCM, and WACCM-fix-EESC Antarctic
446 vortex-average ozone trend profiles in the lower stratosphere for each of the September and
447 October weeks that we analyzed, with triangles marking trends found to be significantly different
448 from zero. The trends for MLS and WACCM that are significantly different from zero are all
449 positive, with the September values peaking at 68 hPa and with somewhat smaller trends in
450 October, which usually brings more perturbed conditions as the vortex weakens. The WACCM
451 simulation with fixed EESC gives results that scatter about zero at lower pressures (higher
452 altitudes) and are generally not significantly different from zero, although there are a few
453 significantly negative values in late October that might be associated with transport-related
454 changes during the more dynamically perturbed conditions. Indeed, even the MLS (panel (a)) and



455 WACCM (panel (b)) results show more variability in the mid-stratosphere, with some non-
456 significant negative late-October trend values.

457 In addition, we tested a regression including a term for the variability that arises at high southern
458 latitudes in connection with the Antarctic Oscillation (AAO), which characterizes atmospheric
459 mass and pressure changes between the southern midlatitudes and the Antarctic region (e.g., Gong
460 and Wang, 1999). More information on the estimation of the AAO index can be found at
461 <https://www.cpc.ncep.noaa.gov/>. The AAO appears to have several multi-year variability
462 components, including a periodicity of about 6 years and other longer-term periodicities (Zhang et
463 al., 2010). If we add the AAO index variation as a function of year to the previously described
464 regression fits, the results are similar to and consistent with the MLR results for MLS, WACCM,
465 and WACCM-fix-EESC shown above, both in terms of trends and their corresponding error bars
466 (Fig. S5). The addition of such a proxy related to AAO variability does not substantially change
467 the total explained variance or the RMS residuals of the fits (not shown).

468 Finally, we comment briefly on the upper stratospheric Antarctic vortex from our simple linear
469 trend analyses, as MLR analyses including a VPSC proxy are not appropriate for that region.
470 Essentially no significant upper stratospheric trends are found for the three weeks in September
471 considered (Fig. S6). The October trends (not shown) are most often not significant in the lower
472 stratosphere and have even more scatter in the upper stratosphere, where MLS and both WACCM
473 simulations show a negative but generally not significant trend. Dynamical changes may be the
474 reason for this behavior, further analysis of which is beyond the scope of this study.

475 **3.2.2 Ozone loss trends from Match analyses of MLS data**

476 We now turn to an ozone trend analysis that focuses more specifically on the winter/spring
477 chemical ozone losses inside the Antarctic vortex and better accounts for transport-related changes,



478 including descent across pressure surfaces or leakage into or out of the vortex. The so-called Match
479 technique was pioneered by von der Gathen et al. (1995), who used multiple ozonesonde profiles
480 within the Arctic vortex to quantify chemical ozone loss. This methodology has been applied (e.g.,
481 Livesey et al., 2015; Santee et al., 2024) to Aura MLS ozone within the polar winter vortices;
482 chemical ozone loss is estimated by tracking a multitude of observed parcels using trajectory
483 calculations along potential temperature surfaces and matching the parcels to subsequent MLS
484 measurements during winter and spring.

485 Figure S7 shows daily cumulative ozone losses for each year from 2005 to 2023 from Match
486 results inside the Antarctic vortex during May to October at four different potential temperature
487 levels between 350 K and 700 K; given that noise in these calculations leads to positive and
488 negative changes in May and June, we focus on the net negative changes (chemical losses), which
489 typically occur after July 1. In October, there can be a slight turnaround in the cumulative changes,
490 as the vortex becomes more affected by mixing across its boundary. The Match profiles of
491 maximum (cumulative) Antarctic ozone loss, which typically occurs in early October (although
492 the date does change from year to year), are shown in Figure 18. Chemical losses as large as 4
493 ppmv are obtained in some of the early years of the Aura mission. As we already mentioned, the
494 well-known September perturbation in 2019 led to some of the weakest ozone destruction in the
495 MLS record, as can also be seen in these plots, where the 2019 maximum lower stratospheric loss
496 only reaches ~2.5 ppmv. The loss values here are slightly different (and generally larger) than the
497 Match-based losses reported by Santee et al. (2024); for the most part, these differences are caused
498 by our use of maximum losses in Fig. 18, rather than calculating the cumulative chemical changes
499 over fixed start and end dates as done by Santee et al., and we also use a more conservative
500 threshold (10% vs. 25%) for the allowed magnitude of along-trajectory PV variability.



501 We then use the ozone loss values for different dates in September and October to calculate
502 weekly average losses, as we did for earlier analyses presented here. A time series example of the
503 inferred chemical losses from 2005 to 2023 for the week centered on September 19 is provided in
504 Figure S8, along with a simple linear fit to that series; the positive trend indicated by this linear fit
505 implies smaller chemical losses over time. Figure 19 shows that, while these linear fits lead to
506 some positive trends in the lower part of the Antarctic vortex, there are also oscillations in the loss
507 profiles, and only a few trends are significantly different from zero; we only show the error bars
508 when the trends are deemed to be significant (i.e., further away from zero than the 2σ error values).
509 We also show the trends obtained from fits to the maximum ozone losses from every year between
510 2005 and 2023; none of these trends are significantly different from zero. Given the small number
511 of Match-derived trends with significant values, we have not pursued any other fits to these
512 chemical ozone loss time series, as we do not expect greater significance from more elaborate
513 MLR fits. The few significant trends obtained from this Match analysis agree, to first order, with
514 the linear trends obtained from our analyses of vortex-average ozone (see the September linear
515 trends in Fig. 12, which are all between 15 and 20 ppbv yr⁻¹). A layer-average of all the September
516 Match trends in chemical ozone loss for potential temperatures below 600 K is slightly less than
517 10 ppbv yr⁻¹ (not shown), which is somewhat smaller than the September vortex-average trends
518 obtained in the previous section.

519 **4 Discussion and Conclusions**

520 Aura MLS measurements of ozone and other species have played a prominent role in the
521 characterization of global stratospheric change since 2004. Here, we have analyzed the MLS
522 distributions of lower stratospheric Antarctic vortex-average ozone profiles from June to



523 November, along with similarly sampled profiles from two WACCM simulations, driven by
524 MERRA-2 meteorological fields with realistic dynamical and temperature information. One of
525 these simulations uses a scheme with surface ODS emissions fixed at 1998 values. These
526 chemistry-climate model simulations include effects from downward transport within the vortex,
527 temperature changes and related changes in PSC activity and heterogeneous chemistry, solar flux
528 and EPP variations, and slow changes in greenhouse gas abundances. Wang et al. (2025) have
529 pointed out that Antarctic ozone changes arising from reductions in ODSs should dominate the
530 impacts from greenhouse gases, for now.

531 The interannual variability in MLS-derived weekly averaged ozone abundances inside the
532 Antarctic vortex is generally well matched by WACCM, although the magnitude of the winter-to-
533 spring ozone decrease is typically slightly smaller in the model. Analyses of probability density
534 functions of ozone profile distributions inside the lower stratospheric Antarctic vortex from 2004
535 to 2023 reveal shifts as a function of year; in particular, there are some relative decreases in the
536 bins with the smallest ozone abundances. The standard WACCM simulation shows similar shifts
537 and good overall agreement with MLS in lower stratospheric vortex-average ozone linear trends
538 from July to November. Such shifts are qualitatively consistent with past findings of changes in
539 ozone loss saturation over Antarctica (Kuttippurath et al., 2018), based mainly on sonde profile
540 data (and partly on MLS data). The fixed-EESC simulation from WACCM shows no significant
541 trends in lower stratospheric ozone and HCl, as one might expect. We also include MLS and
542 WACCM Antarctic vortex profile comparisons for HNO₃; these show good agreement and no
543 significant trends, except for a negative trend in June-July that requires further investigation.

544 As has been commented on previously (WMO, 2022), differences in the various approaches
545 used to quantify Antarctic ozone trends make comparisons of trend estimates from different studies



546 problematic. We note that recent Antarctic vortex analyses by Chang et al. (2025) lead to lower
547 stratospheric vortex-average trends of 10 ppbv yr^{-1} in mid-to-late September and 7 ppbv yr^{-1} in
548 early October, based on MLS ozone data from 2005 to 2022; this is in good accord with our
549 analyses from 2005 to 2023, both in absolute value and in the sense that October shows smaller
550 trends than September, as has been shown previously (WMO, 2022). Wang et al. (2025), who also
551 used MLS profile data but for the 2005 to 2018 period, show reasonable agreement with our linear
552 trend results at some heights, although their average September trend values near 20 to 30 hPa are
553 significantly larger than our weekly mean trends in September. This apparent discrepancy in
554 derived ozone trends is likely largely attributable to differences in the analysis periods used. Also,
555 the 20–30 hPa ($\sim 540\text{--}620 \text{ K}$, $\sim 22\text{--}24 \text{ km}$) layer, which lies just above the region of strongest
556 chemical processing in the heart of the ozone hole, is subject to large interannual variability in the
557 relative interplay between dynamical and chemical effects in September and October. Thus, as
558 illustrated in Fig. S9, it is particularly sensitive to the interval chosen (both start and end dates) for
559 ozone trend estimation; the trend uncertainties are also large in this region.

560 We also used multivariate linear regression fits to weekly mean lower stratospheric vortex-
561 average ozone profiles from MLS and the two WACCM simulations to calculate trends during
562 September and October, when the fastest chemical destruction of ozone occurs. It is useful to
563 analyze both the absolute ozone abundances and the seasonal changes (from early July) in our
564 trend analyses, since both diagnostics should ultimately show robust signs of recovery from the
565 effect of diminishing ODSs. A metric relating to the volume of the sunlit vortex with temperatures
566 low enough to enable NAT PSC formation explains a large part of the year-to-year variability in
567 MLS vortex-average ozone observations. Other proxies used in the regression include two sets of
568 cosine and sine functions with periods of 2.5 and 11 years to represent effects from the quasi-



569 biennial oscillation and longer-term variations, such as the solar cycle (possibly in relation to
570 particle precipitation) or the Antarctic Oscillation; these proxies showed smaller individual
571 impacts on the fits. Reducing the long-term periodicity to 9 or 10 yr does not change the trend
572 results appreciably. Regardless of the exact causal links between geophysical variability and
573 Antarctic vortex ozone, we show that applying MLR analyses rather than simple linear regression
574 decreases lower stratospheric Antarctic ozone trend errors by as much as 40%, while also, as
575 expected, improving the regression fit diagnostics.

576 Overall, our results indicate that lower stratospheric Antarctic ozone values and seasonal
577 changes through mid-September to mid-October are consistent with a slow recovery from the
578 impact of ODSs, with significant positive trends between 5 and 16 ppbv yr⁻¹ at 56 to 100 hPa;
579 trend uncertainties (2σ) range from ~ 8 ppbv yr⁻¹ at 68–56 hPa to ~ 4 ppbv yr⁻¹ at 100 hPa. The
580 WACCM results agree well with those from MLS. As expected, the model simulation with fixed
581 ODS emissions leads to Antarctic ozone trends in the lower stratosphere that are consistent with
582 zero trend. We estimate that the positive ozone trends we obtain for mid-September correspond to
583 an average partial lower stratospheric (pressures larger than 46 hPa) column change of 1 to 1.5 DU
584 yr⁻¹. These values are within the range of Antarctic total column ozone change (~ 25 – 30 DU
585 between 2000 and 2025, or ~ 1 – 1.2 DU yr⁻¹) obtained from various models (e.g., Dhomse et al.,
586 2018; Amos et al., 2020). However, However, partial column ozone changes of this magnitude are
587 still less than half of the amount needed for ozone to return to pre-ozone-hole values over
588 Antarctica, which models predict will occur shortly after mid-century (WMO, 2022).

589 Finally, we explored trends in chemical ozone loss as quantified by the Match technique,
590 whereby MLS measurements of ozone are tracked along trajectories to estimate vortex-average
591 chemical ozone loss during winter/spring. While the Match results show evidence for small



592 reductions in seasonal lower stratospheric Antarctic chemical ozone loss over the 2005 to 2023
593 period, consistent with a positive trend (based on simple linear regression) of order
594 5–15 ppbv yr⁻¹, we obtain statistical significance for only a limited subset of cases in mid-to-late
595 September. There is also a large spread in these trend results as a function of height (potential
596 temperature) inside the vortex. We do not expect that use of a more sophisticated regression fit
597 would produce much improvement in the significance of trends in chemical ozone loss, given the
598 values of the linear-only regression trends and their error bars.

599 These analyses represent new facets of the characterization of the recovery of Antarctic vortex
600 ozone as ODSs diminish, which has been a key goal of the Aura mission. Our results support the
601 robust detection of significant recovery in lower stratospheric Antarctic ozone during parts of
602 September and October over the 2005–2023 period, at pressures larger than 50 hPa. This work
603 adds to the body of evidence underscoring the importance of the 1987 Montreal Protocol and its
604 Amendments, as this international agreement has been a shining example of how policymakers
605 around the world can come together to solve a global environmental problem. However, the
606 upcoming dearth of daily global height-resolved stratospheric composition measurements after the
607 end of the Aura mission (Salawitch et al., 2025) will greatly hinder the ability to detect and
608 understand short- and longer-term changes in stratospheric composition and their effects on the
609 Antarctic ozone hole.

610

611 **Data availability.**

612 The MLS data files are publicly available from the Goddard Earth Sciences Data and Information
613 Services Center (GES DISC) at <https://earthdata.nasa.gov/eosdis/daacs/gesdisc>. The WACCM
614 simulation used here comes from a publicly released version of the Community Earth System



615 Model. Data from the model simulations generated for this work will be made available at the
616 following link (to be added later).

617 **Code availability.** More details to be added later regarding this.

618 **Supplement.** Supplementary material is included.

619

620 **Author contributions.** LF proposed and designed this project, along with (primarily) MJS and
621 DEK; LF also led the writing of this manuscript's first few drafts, along with DEK and MJS. MJS
622 provided analyses and results mostly for the first part of this manuscript (Sect. 3.1), using the
623 WACCM model simulations provided by DEK. LF provided analyses and results mostly for the
624 second part of this manuscript (Sect. 3.2). NJL played a key role in the Match analyses and the
625 interpretation of related seasonal chemical ozone losses. GLM played a key role in the production
626 of files with daily vortex-average quantities, used here for trend analyses. MLS provided detailed
627 comments and helped to improve the manuscript overall. WGR, in part, provided invaluable work
628 towards the creation of the MLS version 5 MLS data used here. RLF mostly provided technical
629 assistance for the datasets and some of the coding used in this work.

630

631 **Competing interests.** The authors declare that they have no conflict of interest.

632

633 **Acknowledgments.** We acknowledge the work of the whole Aura MLS team (past and present)
634 for their various contributions over the years to the mission; special thanks go to Z. D. Lawrence
635 for his contributions to the creation of vortex-related diagnostic quantities. WACCM is
636 a component of the CESM, supported by the National Science Foundation (NSF). We also
637 acknowledge high-performance computing support from Cheyenne (doi:10.5065/D6RX99HX)



638 provided by NCAR's Computational and Information Systems Laboratory, sponsored by the NSF.

639 Work at the Jet Propulsion Laboratory, California Institute of Technology, was performed under

640 contract with the National Aeronautics and Space Administration (80NM0018D0004).

641

642 **Financial support.** LF, MJS, and RAF were funded in part by the NASA Atmospheric

643 Composition Modeling and Analysis Program (ACMAP). NJL, GLM, MLS, and WGR were

644 funded, in part, by the Aura Microwave Limb Sounder project. DEK was funded by NASA and

645 NSF grants. Part of this material is based upon work supported by the NSF National Center for

646 Atmospheric Research, which is a major facility sponsored by the U.S. National Science

647 Foundation under Cooperative Agreement No. 1852977.

648



649 **References**

- 650 Amos, M., Young, P. J., Hosking, J. S., Lamarque, J.-F., Abraham, N. L., Akiyoshi, H., Archibald, A. T.,
651 Bekki, S., Deushi, M., Jöckel, P., Kinnison, D., Kirner, O., Kunze, M., Marchand, M., Plummer, D. A.,
652 Saint-Martin, D., Sudo, K., Tilmes, S., and Yamashita, Y.: Atmos. Chem. Phys., 20, 9961–9977,
653 <https://doi.org/10.5194/acp-20-9661-2020>, 2020.
- 654 Anstey, J. A., Osprey, S. M., Alexander, J., Baldwin, M. P., Butchart, N., Gray, L., Kawatani, Y.,
655 Newman, P. A., and Richter, J. H.: Impacts, processes and projections of the quasi-biennial oscillation,
656 Nature Reviews Earth and Environment, 3, 588–603, <https://doi.org/10.1038/s43017-022-00323-7>,
657 2022.
- 658 Baldwin, M. P., Gray, L. J., Dunkerton, T. J., Hamilton, K., Haynes, P. H., Randel, W. J., Holton, J. R.,
659 Alexander, M. J., Hirota, I., Horinouchi, T., Jones, D. B. A., Kinnersley, J. S., Marquardt, C., Sato, K.,
660 and Takahashi, M.: The quasi-biennial oscillation, Rev. Geophys., 39, 179–
661 229, <https://doi.org/10.1029/1999RG000073>, 2001.
- 662 Burkholder, J. B., Sander, S. P., Abbatt, J. P. D., Barker, J. R., Cappa, C., Crouse, J. D., Dibble, T. S.,
663 Huie, R. E., Kolb, C. E., Kurylo, M. J., Orkin, V. L., Percival, C. J., Wilmouth, D. M., and Wine, P. H.:
664 Chemical kinetics and photochemical data for use in atmospheric studies, Evaluation No. 19, JPL
665 Publication 19-5, Jet Propulsion Laboratory, California Institute of Technology, Pasadena,
666 <http://jpldataeval.jpl.nasa.gov> (last access: 1 December 2022), 2019.
- 667 Chang, J. H.-W., Pien, C. H., Sentian, J., Cordero, R. R., Ooi, M. C.-G., and Wong, Y. J.: Evidence of
668 localized H₂O increases and O₃ recovery in the Antarctic lower stratospheric vortex: MLS observations
669 and BDC variability during late winter to spring, Atmos. Res., 328, 108248,
670 <https://doi.org/10.1016/j.atmosres.2025.108428>, 2025.
- 671 Chipperfield, M. P., Santee, M. L., et al.: Chapter 4, World Meteorological Organization (WMO). Scientific
672 Assessment of Ozone Depletion: 2022, GAW Report No. 278, 509 pp., WMO, Geneva, ISBN: 978-
673 9914-733-97-6, 2022.
- 674 Coddington, O., Lean, J., Pilewskie, P., Snow, M., and Lindholm, D.: A solar irradiance climate data record,
675 B. Am. Meteorol. Soc., 97, 1265–1282, <https://doi.org/10.1175/BAMS-D-14-00265.1>, 2016.
- 676 Danabasoglu, G., Lamarque, J. F., Bacmeister, J., Bailey, D. A., DuVivier, A. K., Edwards, J., Emmons, L.
677 K., Fasullo, J., Garcia, R., Gettelman, A., Hannay, C., Holland, M. M., Large, W. G., Lauritzen, P. H.,
678 Lawrence, D. M., Lenaerts, J. T., Lindsay, K., Lipscomb, W. H., Mills, M. J., Neale, R., Oleson, K.
679 W., Otto-Bliessner, B., Phillips, A. S., Sacks, W., Tilmes, S., van Kampenhout, L., Vertenstein, M.,
680 Bertini, A., Dennis, J., Deser, C., Fischer, C., Fox-Kemper, B., Kay, J. E., Kinnison, D., Kushner, P. J.,
681 Larson, V. E., Long, M. C., Mickelson, S., Moore, J. K., Nienhouse, E., Polvani, L., Rasch, P. J., and



- 682 Strand, W. G.: The Community Earth System Model Version 2 (CESM2), *J. Adv. Model. Earth Syst.*,
683 12, e2019MS001916, <https://doi.org/10.1029/2019MS001916>, 2020.
- 684 Davis, N. A., Callaghan, P., Simpson, I. R., and Tilmes, S.: Specified dynamics scheme impacts on wave-
685 mean flow dynamics, convection, and tracer transport in CESM2 (WACCM6), *Atmos. Chem. Phys.*,
686 22, 197–214, <https://doi.org/10.5194/acp-22-197-2022>, 2022.
- 687 de Laat, A. T. J., van Weele, M., and van der A, R. J.: Onset of stratospheric ozone recovery in the Antarctic
688 ozone hole in assimilated daily total ozone columns, *J. Geophys. Res.*, 122, 11,880–11,899,
689 <https://doi.org/10.1002/2016JD025723>, 2017.
- 690 Dhomse, S. S., Kinnison, D., Chipperfield, M. P., Salawitch, R. J., Cionni, I., Hegglin, M. I., Abraham, N.
691 L., Akiyoshi, H., Archibald, A. T., Bednarz, E. M., Bekki, S., Braesicke, P., Butchart, N., Dameris, M.,
692 Deushi, M., Frith, S., Hardiman, S. C., Hassler, B., Horowitz, L. W., Hu, R.-M., Jöckel, P., Josse, B.,
693 Kirner, O., Kremser, S., Langematz, U., Lewis, J., Marchand, M., Lin, M., Mancini, E., Marécal, V.,
694 Michou, M., Morgenstern, O., O'Connor, F. M., Oman, L., Pitari, G., Plummer, D. A., Pyle, J. A.,
695 Revell, L. E., Rozanov, E., Schofield, R., Stenke, A., Stone, K., Sudo, K., Tilmes, S., Visioni, D.,
696 Yamashita, Y., and Zeng, G.: Estimates of ozone return dates from Chemistry-Climate Model Initiative
697 simulations, *Atmos. Chem. Phys.*, 18, 8409–8438, <https://doi.org/10.5194/acp-18-8409-2018>, 2018.
- 698 Emmons, L. K., Schwantes, R. H., Orlando, J. J., Tyndall, G., Kinnison, D., Lamarque, J.-F., Marsh, D.,
699 Mills, M. J., Tilmes, S., Bardeen, C., Buchholz, R. R., Conley, A., Gettelman, A., Garcia, R., Simpson,
700 I., Blake, D. R., Meinardi, S., and Pétron, G.: The Chemistry Mechanism in the Community Earth
701 System Model version 2 (CESM2), *J. Adv. Model. Earth Syst.*, 12, e2019MS001882,
702 <https://doi.org/10.1029/2019MS001882>, 2020.
- 703 Engel, A., Bönisch, H., Ostermüller, J., Chipperfield, M. P., Dhomse, S., and Jöckel, P.: A refined method
704 for calculating equivalent effective stratospheric chlorine, *Atmos. Chem. Phys.*, 18, 601–
705 619, <https://doi.org/10.5194/acp-18-601-2018>, 2018.
- 706 Farman, J. C., Gardiner, B. G., and Shanklin, J. D.: Large losses of total ozone in Antarctica reveal seasonal
707 ClO_x/NO_x interaction, *Nature*, 315, 207–210, 1985.
- 708 Froidevaux, L., Jiang, Y. B., Lambert, A., Livesey, N. J., Read, W. G., Waters, J. W., Browell, E. V., Hair,
709 J. W., Avery, M. A., McGee, T. J., Tiwgg, L. W., Sunnicht, G. K., Jucks, K. W., Margitan, J. J., Sen,
710 B., Stachnik, R. A., Toon, G. C., Bernath, P. F., Boone, C. D., Walker, K. A., Filipiak, M. J., Harwood,
711 R. S., Fuller, R. A., Manney, G. L., Schwartz, M. J., Daffer, W. H., Drouin, B. J., Cofield, R. E., Cuddy,
712 D. T., Jarnot, R. F., Knosp, B. W., Perun, V. S., Snyder, W. V., Stek, P. C., Thurstans, R. P., and Wagner,
713 P. A.: Validation of Aura Microwave Limb Sounder stratospheric and mesospheric ozone
714 measurements, *J. Geophys. Res.*, 113, D15S20, doi:10.1029/2007JD008771, 2008.



- 715 Gelaro, R., McCarty, W., Suarez, M. J., Todling, R., Molod, A., Takacs, L., Randles, C. A., Darmenov,
716 A., Bosilovich, M. G., Reichle, R., Wargan, K., Coy, L., Cullather, R., Draper, C., Akella,
717 S., Buchard, V., Conaty, A., da Silva, A. M., Gu, W., Kim, G.-K., Koster, R., Lucchesi, R., Merkova,
718 D., Nielsen, J. E., Partyka, G., Pawson, S., Putman, W., Rienecker, M., Schubert, S. D., Sienkiewicz,
719 M., and Zhao, B.: The Modern-Era Retrospective Analysis for Research and Applications, Version 2
720 (MERRA2), *J. Clim.*, 30, 5419–5454, <https://doi.org/10.1175/JCLI-D-16-0758.1>, 2017.
- 721 Gettelman, A., Mills, M. J., Kinnison, D. E., Garcia, R. R., Smith, A. K., Marsh, D. R., Tilmes, S., Vitt, F.,
722 Bardeen, C. G., McInerney, J., Liu, H. L., Solomon, S. C., Polvani, L. M., Emmons, L. K., Lamarque, J.
723 F., Richter, J. H., Glanville, A. S., Bacmeister, J. T., Phillips, A. S., Neale, R. B., Simpson, I. R.,
724 DuVivier, A. K., Hodzic, A., and Randel, W. J.: The Whole Atmosphere Community Climate Model
725 Version 6 (WACCM6), *J. Geophys. Res.-Atmos.*, 124, 12380–12403,
726 <https://doi.org/10.1029/2019JD030943>, 2019.
- 727 Gong, D., and Wang, S.: Definition of Antarctic oscillation index, *Geophys. Res. Lett.*, 26, 4, 459-462,
728 <https://doi.org/10.1029/1999GL900003>, 1999.
- 729 Gordon, E.M., A. Seppälä, B. Funke, J. Tamminen, and K.A. Walker, Observational evidence of energetic
730 particle precipitation NO_x (EPP-NO_x) interaction with chlorine curbing Antarctic ozone loss, *Atmos.*
731 *Chem. Phys.*, 21, 2819–2836, doi:10.5194/acp-21-2819-2021, 2021.
- 732 Grooss, J.-U., Müller, R., Crowley, J. N., and Hegglin, M. I.: Chlorine peroxide reaction explains observed
733 wintertime hydrogen chloride in the Antarctic vortex, *Nature Commun. Earth Environ.*, 6, 496,
734 <https://doi.org/10.1038/s43247-025-02499-4>, 2025.
- 735 Hubert, D., Lambert, J.-C., Verhoelst, T., Granville, J., Keppens, A., Baray, J.-L., Bourassa, A. E., Cortesi,
736 U., Degenstein, D. A., Froidevaux, L., Godin-Beekmann, S., Hoppel, K. W., Johnson, B. J., Kyrölä, E.,
737 Leblanc, T., Lichtenberg, G., Marchand, M., McElroy, C. T., Murtagh, D., Nakane, H., Portafaix, T.,
738 Querel, R., Russell III, J. M., Salvador, J., Smit, H. G. J., Stebel, K., Steinbrecht, W., Strawbridge, K.
739 B., Stübi, R., Swart, D. P. J., Taha, G., Tarasick, D. W., Thompson, A. M., Urban, J., van Gijssel, J. A.
740 E., Van Malderen, R., von der Gathen, P., Walker, K. A., Wolfram, E., and Zawodny, J. M.: Ground-
741 based assessment of the bias and long-term stability of 14 limb and occultation ozone profile data
742 records, *Atmos. Meas. Tech.*, 9, 2497–2534, <https://doi.org/10.5194/amt-9-2497-2016>, 2016.
- 743 Jackman, C. H., Marsh, D. R., Vitt, F. M., Garcia, R. R., Randall, C. E., Fleming, E. L., and Frith, S. M.:
744 Long-term middle atmospheric influence of very large solar proton events, *J. Geophys. Res.*, 114,
745 D11304, <https://doi.org/10.1029/2008JD011415>, 2009.
- 746 Jiang, Y. B., Froidevaux, L., Lambert, A., Livesey, N. J., Read, W. G., Waters, J. W., Bojkov, B., Leblanc,
747 T., McDermid, I. S., Godin-Beekmann, S., Filipiak, M. J., Harwood, R. S., Fuller, R. A., Daffer, W. H.,
748 Drouin, B. J., Cofield, R. E., Cuddy, D. T., Jarnot, R. F., Knosp, B. W., Perun, V. S., Schwartz, M. J.,



- 749 Snyder, W. V., Stek, P. C., Thurstans, R. P., Wagner, P. A., Allaart, M., Andersen, S. B., Bodeker, G.,
750 Calpini, B., Claude, H., Coetzee, G., Davies, J., De Backer, H., Dier, H., Fujiwara, M., Johnson, B.,
751 Kelder, H., Leme, N. P., Koenig-Langlo, G., Kyro, E., Laneve, G., Fook, L. S., Merrill, J., Morris, G.,
752 Newchurch, M., Oltmans, S., Parrondos, M. C., Posny, F., Schmidlin, F., Skrivankova, P., Stubi, R.,
753 Tarasick, D., Thompson, A., Thouret, V., Viatte, P., Vomel, H., von Der Gathen, P., Yela, M., and
754 Zablocki, G.: Validation of the Aura Microwave Limb Sounder Ozone by ozonesonde and lidar
755 measurements, *J. Geophys. Res.*, 112, D24S34, doi:10.1029/2007JD008776, 2007.
- 756 Kessenich, H., Seppala, A., and Rodger, C.: Potential drivers of the recent large Antarctic ozone
757 holes, *Nature Comm.*, 14, 1, doi:10.1038/s41467-023-42637-0, 2023.
- 758 Kinnison, D. E., Brasseur, G. P., Walters, S., Garcia, R. R., Marsh, D. R., Sassi, F., Harvey, V. L., Randall,
759 C. E., Emmons, L., Lamarque, J. F., Hess, P., Orlando, J. J., Tie, X. X., Randel, W., Pan, L. L.,
760 Gettelman, A., Granier, C., Diehl, T., Niemeier, U., and Simmons, A. J.: Sensitivity of chemical tracers
761 to meteorological parameters in the MOZART-3 chemical transport model, *J. Geophys. Res.-Atmos.*,
762 112, 20302, <https://doi.org/10.1029/2006JD007879>, 2007.
- 763 Kuttippurath, J., Godin-Beekmann, S., Lefèvre, F., Santee, M. L., Froidevaux, L., and Hauchecorne, A.,
764 Variability in Antarctic ozone loss in the last decade (2004–2013): high-resolution simulations
765 compared to Aura MLS observations, *Atmos. Chem. Phys.*, 15, 10385–10397, doi:10.5194/acp-15-
766 10385-2015, 2015.
- 767 Kuttippurath, J., Kumar, P., Nair, P.J., and Pandey, P.: Emergence of ozone recovery evidenced by
768 reduction in the occurrence of Antarctic ozone loss saturation, *Clim. Atmos. Sci.*, 1, 42 (2018).
769 <https://doi.org/10.1038/s41612-018-0052-6>, 2018.
- 770 Lawrence, Z. D., Manney, G. L., Minschwaner, K., Santee, M. L., and Lambert, A.: Comparisons of polar
771 processing diagnostics from 34 years of the ERA-Interim and MERRA reanalyses,
772 *Atmos. Chem. Phys.*, 15, 3873–3892, <https://doi.org/10.5194/acp-15-3873-2015>, 2015.
- 773 Lawrence, Z. D., Manney, G. L., & Wargan, K.: Reanalysis intercomparisons of stratospheric polar
774 processing diagnostics, *Atmos. Chem. Phys.*, 18, 13547–13579, [https://doi.org/10.5194/acp-18-13547-](https://doi.org/10.5194/acp-18-13547-2018)
775 [2018](https://doi.org/10.5194/acp-18-13547-2018), 2018.
- 776 Lickley, M. J., Daniel, J. S., McBride, L. A., Salawitch, R. J., and Velders, G. J. M.: The return to 1980
777 stratospheric halogen levels: a moving target in ozone assessments from 2006 to 2022, *Atmos. Chem.*
778 *Phys.*, 24, 13081–13099, <https://doi.org/10.5194/acp-24-13081-2024>, 2024.
- 779 Livesey, N. J., and Read, W. G.: Direct retrieval of line-of-sight atmospheric structure from limb sounding
780 observations, *Geophys. Res. Lett.*, 27, 891-894, <https://doi.org/10.1029/1999GL010964>, 2000.



- 781 Livesey, N. J., Snyder, W. V., Read, W. G., and Wagner, P. A.: Retrieval algorithms for the EOS
782 Microwave Limb Sounder (MLS), *IEEE T. Geosci. Remote*, 44, 1144–1155,
783 doi:10.1109/TGRS.2006.872327, 2006.
- 784 Livesey, N. J., Filipiak, M. J., Froidevaux, L., Read, W. G., Lambert, A., Santee, M. L., Jiang, J. H., Waters,
785 J. W., Cofield, R. E., Cuddy, D. T., Daffer, W. H., Drouin, B. J., Fuller, R. A., Jarnot, R. F., Jiang, Y.
786 B., Knosp, B. W., Li, Q. B., Perun, V. S., Schwartz, M. J., Snyder, W. V., Stek, P. C., Thurstans, R. P.,
787 Wagner, P. A., Pumphrey, H. C., Avery, M., Browell, E. V., Cammas, J.-P., Christensen, L. E., Edwards,
788 D. P., Emmons, L. K., Gao, R.-S., Jost, H.-J., Loewenstein, M., Lopez, J. D., Nédélec, P., Osterman, G.
789 B., Sachse, G. W., and Webster, C. R.: Validation of Aura Microwave Limb Sounder O₃ and CO
790 observations in the upper troposphere and lower stratosphere, *J. Geophys. Res.*, 113, D15S02,
791 doi:10.1029/2007JD008805, 2008.
- 792 Livesey, N. J., Santee, M. L., and Manney, G. L.: A Match-based approach to the estimation of polar
793 stratospheric ozone loss using Aura Microwave Limb Sounder observations, *Atmos. Chem. Phys.*, 15,
794 9945–9963, doi:10.5194/acp-15-9945-2015, 2015.
- 795 Livesey, N. J., Read, W. G., Wagner, P. A., Froidevaux, L., Santee, M. L., Schwartz, M. J., Lambert, A.,
796 Millan Valle, L. F., Pumphrey, H. C., Manney, G. L., Fuller, R. A., Jarnot, R. F., Knosp, B. W., and
797 Lay, R. R.: EOS MLS Version 5.0x Level 2 and 3 data quality and description document, Tech. rep., Jet
798 Propulsion Laboratory D-105336 Rev. B, Jan. 30, 2022, <https://mls.jpl.nasa.gov/eos-aura-mls/documentation.php>, 2022.
- 800 Mahieu, E., Chipperfield, M. P., Notholt, J., Reddmann, T., Anderson, J., Bernath, P. F., Blumenstock, T.,
801 Coffey, M. T., Dhomse, S. S., Feng, W., Franco, B., Froidevaux, L., Griffith, D. W. T., Hannigan, J.
802 W., Hase, F., Hossaini, R., Jones, N. B., Morino, I., Murata, I., Nakajima, H., Palm, M., Paton-Walsh,
803 C., Russell III, J. M., Schneider, M., Servais, C., Smale, D., and Walker, K.: Recent northern hemisphere
804 stratospheric HCl increase due to atmospheric circulation changes, *Nature*, 515(7525), 104–107,
805 <https://doi.org/10.1038/nature13857>, 2014.
- 806 Maliniemi, V., Arsenovic, P., Seppälä, A., and Nesse Tyssøy, H.: The influence of energetic particle
807 precipitation on Antarctic stratospheric chlorine and ozone over the 20th century, *Atmos. Chem. Phys.*
808 22, 8137–8149, 2022.
- 809 Manney, G. L., Santee, M. L., Rex, M., Livesey, N. J., Pitts, M. C., Veefkind, P., et al., Unprecedented
810 Arctic ozone loss in 2011, *Nature*, 478(7370), 469–475. <https://doi.org/10.1038/nature10556>, 2011.
- 811 Manney, G. L., Santee, M. L., Lambert, A., Millán, L. F., Minschwaner, K., Werner, F., Lawrence, Z. D.,
812 Read, W. G., Livesey, N. J., and Wang, T.: Siege in the southern stratosphere: HungaTonga–Hunga
813 Ha’apai water vapor excluded from the 2022 Antarctic polar vortex, *Geophys. Res. Lett.*, 50(14),
814 e2023GL103855, <https://doi.org/10.1029/2023GL103855>, 2023.



- 815 Matthes, K., Funke, B., Andersson, M. E., Barnard, L., Beer, J., Charbonneau, P., Clilverd, M. A., Dudok
816 de Wit, T., Haberreiter, M., Hendry, A., Jackman, C. H., Kretzschmar, M., Kruschke, T., Kunze, M.,
817 Langematz, U., Marsh, D. R., Maycock, A. C., Misios, S., Rodger, C. J., Scaife, A. A., Seppälä, A.,
818 Shangguan, M., Sinnhuber, M., Tourpali, K., Usoskin, I., van de Kamp, M., Verronen, P. T.,
819 and Versick, S.: Solar forcing for CMIP6 (v3.2), *Geoscientific Model Development*, 10(6), 2247–
820 2302, <https://doi.org/10.5194/gmd-10-2247-2017>, 2017.
- 821 Meinshausen, M., Vogel, E., Nauels, A., Lorbacher, K., Meinshausen, N., Etheridge, D. M., Fraser, P. J.,
822 Montzka, S. A., Rayner, P. J., Trudinger, C. M., Krumme, P. B., Beyerle, U., Canadell, J. G., Daniel, J.
823 S., Enting, I. G., Law, R. M., Lunder, C. R., O’Doherty, S., Prinn, R. G., Reimann, S., Rubino, M.,
824 Velders, G. J. M., Vollmer, M. K., Wang, R. H.-J., and Weiss, R.: Historical greenhouse gas
825 concentrations for climate modelling (CMIP6), *Geoscientific Model Development*, 10(5), 2057–2116.
826 <https://doi.org/10.5194/gmd-10-2057-2017>, 2017.
- 827 Meinshausen, M., Nicholls, Z. R. J., Lewis, J., Gidden, M. J., Vogel, E., Freund, M., Beyerle, U., Gessner,
828 C., Nauels, A., Bauer, N., Canadell, J. G., Daniel, J. S., John, A., Krummel, P. B., Luderer, G.,
829 Meinshausen, N., Montzka, S. A., Rayner, P. J., Reimann, S., Smith, S. J., van den Berg, M., Velders,
830 G. J. M., Vollmer, M. K., and Wang, R. H. J.: The shared socio-economic pathway (SSP) greenhouse
831 gas concentrations and their extensions to 2500, *Geosci. Model Dev.*, 13, 3571–
832 3605, <https://doi.org/10.5194/gmd-13-3571-2020>, 2020.
- 833 Neely, R. R. and Schmidt, A.: VolcanEESM: Global volcanic sulphur dioxide (SO₂) emissions database
834 from 1850 to present – Version 1.0., <https://doi.org/10.5285/76ebdc0b-0eed-4f70-b89e-55e606bcd568>,
835 2016.
- 836 Newman, P. A., Daniel, J. S., Waugh, D. W., and Nash, E. R.: A new formulation of equivalent effective
837 stratospheric chlorine (EESC), <https://doi.org/10.5194/acp-7-4537-2007>, 2007.
- 838 O’Neill, B. C., Tebaldi, C., van Vuuren, D. P., Eyring, V., Friedlingstein, P., Hurtt, G., Knutti, R., Kriegler,
839 E., Lamarque, J.-F., Lowe, J., Meehl, G. A., Moss, R., Riahi, K., and Sanderson, B. M.: The Scenario
840 Model Intercomparison Project (ScenarioMIP) for CMIP6, *Geosci. Model Dev.*, 9, 3461–3482,
841 <https://doi.org/10.5194/gmd-9-3461-2016>, 2016.
- 842 Pazmiño, A., Godin-Beekmann, S., Hauchecorne, A., Claud, C., Khaykin, S., Goutail, F., Wolfram, E.,
843 Salvador, J., and Quel, E.: Multiple symptoms of total ozone recovery inside the Antarctic vortex during
844 austral spring, *Atmos. Chem. Phys.*, 18, 7557–7572, <https://doi.org/10.5194/acp-18-7557-2018>, 2018.
- 845 Pazmiño, A., Goutail, F., Sophie Godin-Beekmann, S., Hauchecorne, A., Pommereau, J.-P., Chipperfield,
846 M. P., Feng, W., Franck Lefèvre, F., Lecouffe, A., Van Roozendaal, M., Jepsen, N., Hansen, G., Rigel
847 Kivi, R., Kimberly Strong, K., and Walker, K. A.: Trends in polar ozone loss since 1989: potential sign



- 848 of recovery in the Arctic ozone column, *Atmos. Chem. Phys.*, 23, 15655–15670,
849 <https://doi.org/10.5194/acp-23-15655-2023>, 2023.
- 850 Read, W. G., Shippony, Z., and Snyder, W. V.: The clear-sky unpolarized forward model for the EOS Aura
851 microwave limb sounder (MLS), *IEEE Trans. Geosci. Remote Sens.*, 44, 1367–1379,
852 <https://doi.org/10.1109/TGRS.2006.862267>, 2006.
- 853 Rex, M., Salawitch, R. J., von der Gathen, P., Harris, N. R. P., Chipperfield, M. P., and Naujokat, B.: Arctic
854 ozone loss and climate change, *Geophys. Res. Lett.*, 31, L04116,
855 doi:10.1029/2003GL018844, 2004.
- 856 Riahi, K., van Vuuren, D. P., Kriegler, E., Edmonds, J., O’Neill, B. C., Fujimori, S., Bauer, N., Calvin, K.,
857 Dellink, R., Fricko, O., Lutz, W., Popp, A., Crespo Cuaresma, J., Samir, K. C., Leimbach, M., Jiang, L.,
858 Kram, T., Rao, S., Emmerling, J., Ebi, K., Hasegawa, T., Havlik, P., Humpenöder, F., Da Silva, A.,
859 Smith, S., Stehfest, E., Bosetti, V., Eom, J., Gernaat, D., Masui, T., Rogelj, J., Strefler, J., Drouet, L.,
860 Krey, V., Luderer, G., Harmsen, M., Takahashi, K., Baumstark, L., Doelman, J. C., Kainuma, M.,
861 Klimont, Z., Marangoni, G., Lotze-Campen, H., Obersteiner, M., Tabeau, A., and Tavoni, M.: The
862 Shared Socioeconomic Pathways and their energy, land use, and greenhouse gas emissions implications:
863 An overview, *Global Environ. Chang.*, 42, 1045–1058, <https://doi.org/10.1016/j.gloenvcha.2016.05.009>, 2017.
- 865 Rodgers, C.: *Inverse Methods for Atmospheric Sounding: Theory and Practice*, Vol. 2 of Series on
866 Atmospheric, Oceanic and Planetary Physics, World Scientific, Singapore, 2000.
- 867 Roy, R., Kumar, P., Kuttippurath, J., and Lefèvre, F.: Chemical ozone loss and chlorine activation in the
868 Antarctic winters of 2013–2020, *Atmos. Chem. Phys.*, 24, 2377–2386, [https://doi.org/10.5194/acp-24-](https://doi.org/10.5194/acp-24-2377-2024)
869 [2377-2024](https://doi.org/10.5194/acp-24-2377-2024), 2024.
- 870 Salawitch, R., Smith, J., Selkirk, H., Wargan, K., Chipperfield, M., Hossaini, R., Levelt, P., Livesey, N. J.,
871 McBride, L., Millan, L., Moyer, E., Santee, M. L., Schoeberl, M., Solomon, S., Stone, K., and Worden,
872 H.: The Imminent Data Desert: The Future of Stratospheric Monitoring in a Rapidly Changing
873 World, *Bull. Am. Meteorol. Soc.*, 106, 3, E540–E563, [doi:10.1175/bams-d-23-0281.1](https://doi.org/10.1175/bams-d-23-0281.1), 2025.
- 874 Santee, M. L., Manney, G. L., Livesey, N. J. J., Froidevaux, L., MacKenzie, I. A., Pumphrey, H. C., Read,
875 W. G., Schwartz, M. J., Waters, J. W., and Harwood, R. S.: Polar processing and development of the
876 2004 Antarctic ozone hole: first results from MLS on Aura, *Geophys. Res. Lett.*, 32, L12817,
877 doi:10.1029/2005GL022582, 2005.
- 878 Santee, M. L., Manney, G. L., Livesey, N. J., Froidevaux, L., Schwartz, M. J., and Read, W. G.: Trace gas
879 evolution in the lowermost stratosphere from Aura Microwave Limb Sounder measurements, *J.*
880 *Geophys. Res.*, 116, D18306, doi:10.1029/2011JD015590, 2011.



- 881 Santee, M. L., Manney, G. L., Lambert, A., Millán, L. F., Livesey, N. J., Pitts, M. C., Froidevaux, L., Read,
882 W. G., and Fuller, R. A.: The Influence of Stratospheric Hydration From the Hunga Eruption on
883 Chemical Processing in the 2023 Antarctic Vortex, *Journal of Geophysical Research: Atmospheres*, 129,
884 e2023JD040687, <https://doi.org/10.1029/2023JD040687>, 2024.
- 885 Solomon, S.: Stratospheric ozone depletion: A review of concepts and history, *Rev. Geophys.*, 37, 275–
886 316, doi:10.1029/1999RG900008, 1999.
- 887 Solomon, S., D. Kinnison, J. Bandoro, and R. Garcia, Simulation of polar ozone depletion: An update, *J.*
888 *Geophys. Res. Atmos.*, 120, 7958–7974, doi:10.1002/2015JD023365, 2015.
- 889 Solomon, S., Ivy, D. J., Kinnison, D., Nills, M. J., Neely, R. R., and Schmidt, A.: Emergence of healing in
890 the Antarctic ozone layer, *Science*, 353 (6296), 269–274, doi:10.1126/science.aae0061, 2016.
- 891 Strahan, S. E., Douglass, A. R., Newman, P. A., and Steenrod, S. D.: Inorganic chlorine variability in the
892 Antarctic vortex and implications for ozone recovery, *J. Geophys. Res. Atmos.*, 119, 14,098–14,109,
893 <https://doi.org/10.1002/2014JD022295>, 2014.
- 894 Strahan, S. E., and Douglass, A. R.: Decline in Antarctic ozone depletion and lower stratospheric chlorine
895 determined from Aura Microwave Limb Sounder observations. *Geophys. Res. Lett.*, 45, 382–390,
896 <https://doi.org/10.1002/2017GL074830>, 2018.
- 897 Strahan, S. E., Douglass, A. R., and Damon, M. R.: Why do Antarctic ozone recovery trends vary?, *J.*
898 *Geophys. Res.-Atmos.*, 124, 8837–8850, <https://doi.org/10.1029/2019JD030996>, 2019.
- 899 Strahan, S. E., Smale, D., Douglass, A. R., Blumenstock, T., Hannigan, J. W., Hase, F., Jones, N. B.,
900 Mahieu, E., Notholt, J., Oman, L. D., Ortega, I., Palm, M., Prignon, M., Robinson, J., Schneider, M.,
901 Sussmann, R., and Velasco, V. A.: Observed hemispheric asymmetry in stratospheric transport trends
902 from 1994 to 2018, *Geophys. Res. Lett.*, 47, e2020GL088567, <https://doi.org/10.1029/2020GL088567>,
903 2020.
- 904 Tilmes, S., Muller, R., Grooß, J.-U., and Russell, J. M.: Ozone loss and chlorine activation in the Arctic
905 winters 1991–2003 derived with the tracer-tracer correlations, *Atmos. Chem. Phys.*, 4, 2181–2213,
906 <http://www.atmos-chem-phys.net/4/2181/2004/>, 2004.
- 907 von der Gathen, P., Rex, M., Harris, N. R. P., Lucic, D., Knudsen, B. M., Braathen, G. O., de Backer, H.,
908 Fabian, R., Fast, H., Gil, M., Kyrö, E., Mikkelsen, I. S., Rummukainen, M., Stähelin, J., and Varotsos,
909 C.: Observational evidence for chemical ozone depletion over the Arctic in winter 1991–92, *Nature*,
910 375, 131–134, 1995.
- 911 Wang, P., Solomon, S., Santer, B. D., Kinnison, D. E., Fu, Q., Stone, K. A., Zhang, J., Manney, G. L., and
912 Millan, L. F.: Fingerprinting the recovery of Antarctic ozone, *Nature*, 649, 646–651,
913 <https://doi.org/10.1038/s41586-025-08640-9>, 2025.



- 914 Wargan, K., Weir, B., Manney, G. L., Cohn, S., and Livesey, N. J.: The anomalous 2019 Antarctic ozone
915 hole in the GEOS Constituent Data Assimilation System with MLS observations, *J. Geophys. Res.-*
916 *Atmos.*, 125, e2020JD033335, <https://doi.org/10.1029/2020JD033335>, 2020.
- 917 Waters, J., Froidevaux, L., Harwood, R., Jarnot, R., Pickett, H., Read, W., Siegel, P., Cofield, R., Filipiak,
918 M., Flower, D., Holden, J., Lau, G., Livesey, N., Manney, G., Pumphrey, H., Santee, M., Wu, D., Cuddy,
919 D., Lay, R., Loo, M., Perun, V., Schwartz, M., Stek, P., Thurstans, R., Boyles, M., Chandra, S., Chavez,
920 M., Chen, G.-S., Chudasama, B., Dodge, R., Fuller, R., Girard, M., Jiang, J., Jiang, Y., Knosp, B.,
921 LaBelle, R., Lam, J., Lee, K., Miller, D., Oswald, J., Patel, N., Pukala, D., Quintero, O., Scaff, D.,
922 Snyder, V., Tope, M., Wagner, P., and Walch, M.: The Earth Observing System Microwave Limb
923 Sounder (EOS MLS) on the Aura satellite, *IEEE Transac. Geosci. Remote Sens.*, 44, 5,
924 <https://doi.org/10.1109/TGRS.2006.873771>, 2006.
- 925 Weber, M., Coldewey-Egbers, M., Fioletov, V. E., Frith, S. M., Wild, J. D., Burrows, J. P., Long, C. S.,
926 and Loyola, D.: Total ozone trends from 1979 to 2016 derived from five merged observational datasets
927 – the emergence into ozone recovery, *Atmos. Chem. Phys.*, 18, 2097–2117, [https://doi.org/10.5194/acp-](https://doi.org/10.5194/acp-18-2097-2018)
928 [18-2097-2018](https://doi.org/10.5194/acp-18-2097-2018), 2018.
- 929 Wegner, T., Kinnison, D. E., Garcia, R. R., and Solomon, S.: Simulation of polar stratospheric clouds in
930 the specified dynamics version of the whole atmosphere community climate model, *J. Geophys. Res.-*
931 *Atmos.*, 118, 4991–5002, <https://doi.org/10.1002/jgrd.50415>, 2013.
- 932 Weimer, M., Kinnison, D. E., Wilka, C., and Solomon, S.: Effects of denitrification on the distributions of
933 trace gas abundances in the polar regions: a comparison of WACCM with observations, *Atmos. Chem.*
934 *Phys.*, 23, <https://doi.org/10.5194/acp-23-6849-2023>, 2023.
- 935 Wilka, C., Solomon, S., Kinnison, D., and Tarasick, D.: An Arctic ozone hole in 2020 if not for the Montreal
936 Protocol, <https://doi.org/10.5194/acp-21-15771-2021>, 2021.
- 937 WMO: Scientific Assessment of Ozone Depletion: 2018, Global Ozone Research and Monitoring Project–
938 Report No. 58, 588 pp., WMO, Geneva, Switzerland, ISBN: 978-1-7329317-1- 8, 2018.
- 939 WMO: Scientific Assessment of Ozone Depletion: 2022, GAW Report No. 278, 509 pp., WMO, Geneva,
940 Switzerland, ISBN: 978-9914-733-97-6, 2022.
- 941 Zhang, Z.-Y., Gong, D.-Y., He, X.-Z., Lei, Y.-N., and Feng, S.-H.: Statistical reconstruction of the Antarctic
942 Oscillation Index based on multiple proxies, *Atmos. Ocean. Sci. Lett.*, 3, 5, 283-287,
943 <https://doi.org/10.1080/16742834.2010.11446883>, 2010.
- 944 Ziemke, J. R., Oman, L. D., Strode, S. A., Douglass, A. R., Olsen, M. A., McPeters, R. D., Bhartia, P. K.,
945 Froidevaux, L., Labow, G. J., Witte, J. C., Thompson, A. M., Haffner, D. P., Kramarova, N. A., Frith,
946 S. M., Huang, L.-K., Jaross, G. R., Seftor, C. J., Deland, M. T., and Taylor, S. L.: Trends in global
947 tropospheric ozone inferred from a composite record of TOMS/OMI/MLS/OMPS satellite

<https://doi.org/10.5194/egusphere-2026-2273>

Preprint. Discussion started: 29 April 2026

© Author(s) 2026. CC BY 4.0 License.



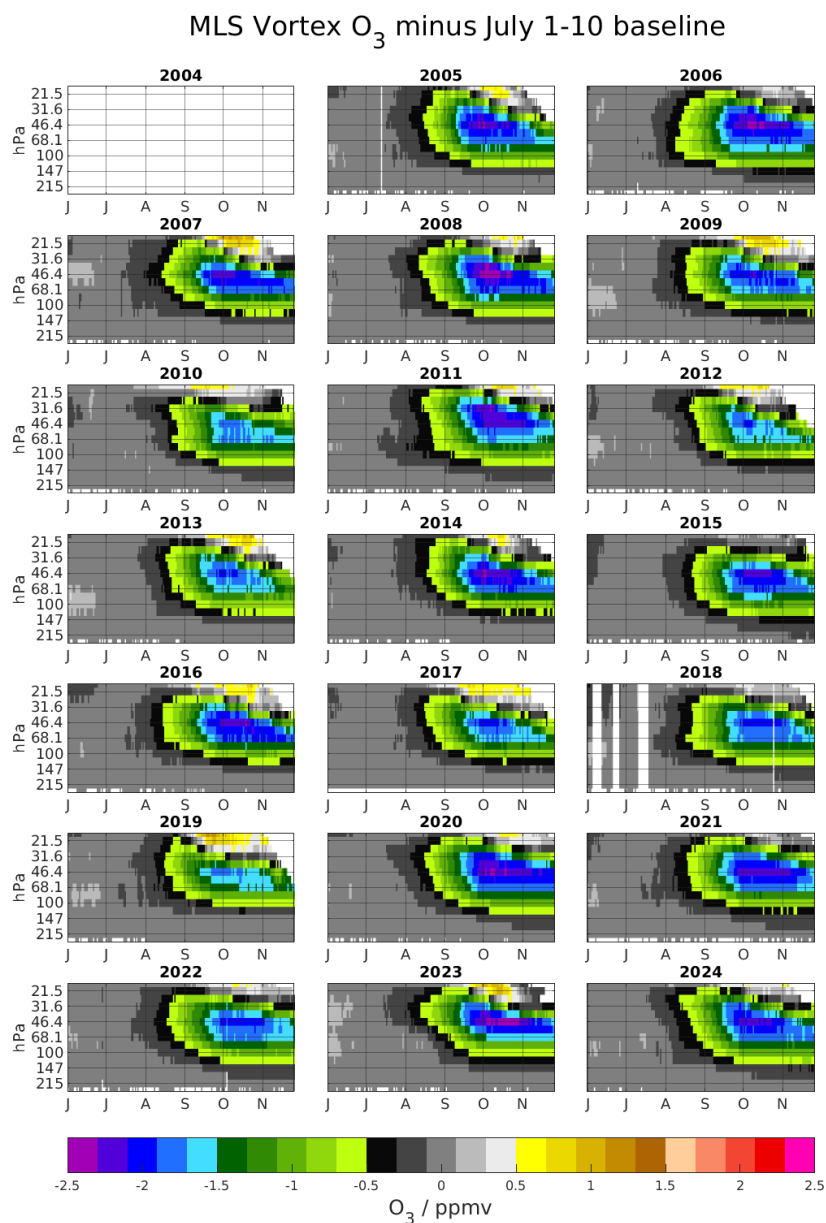
948 measurements and the MERRA-2 GMI simulation, *Atmos. Chem. Phys.*, 19, 3257–3269,

949 <https://doi.org/10.5194/acp-19-3257-2019>, 2019.

950



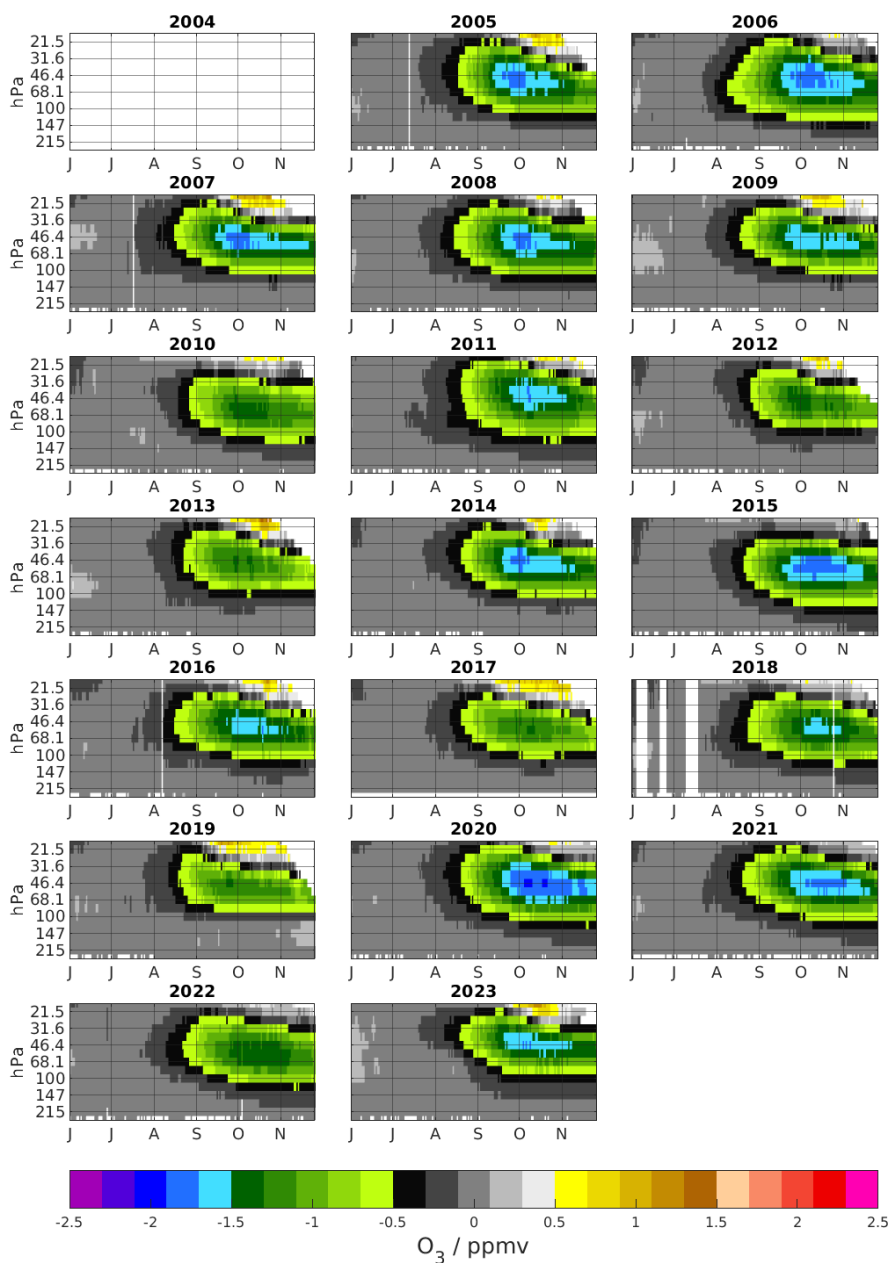
951 **Figures**



952 **Figure 1.** June to November vortex-average lower stratospheric ozone profiles over the range 215–
953 21 hPa for 2005–2024. The respective July 1–10 average is subtracted for each year to remove
954 interannual variability of early-winter (baseline) conditions. Partial 2004 is not included because
955 MLS operations had not begun in July, so this baseline could not be calculated
956

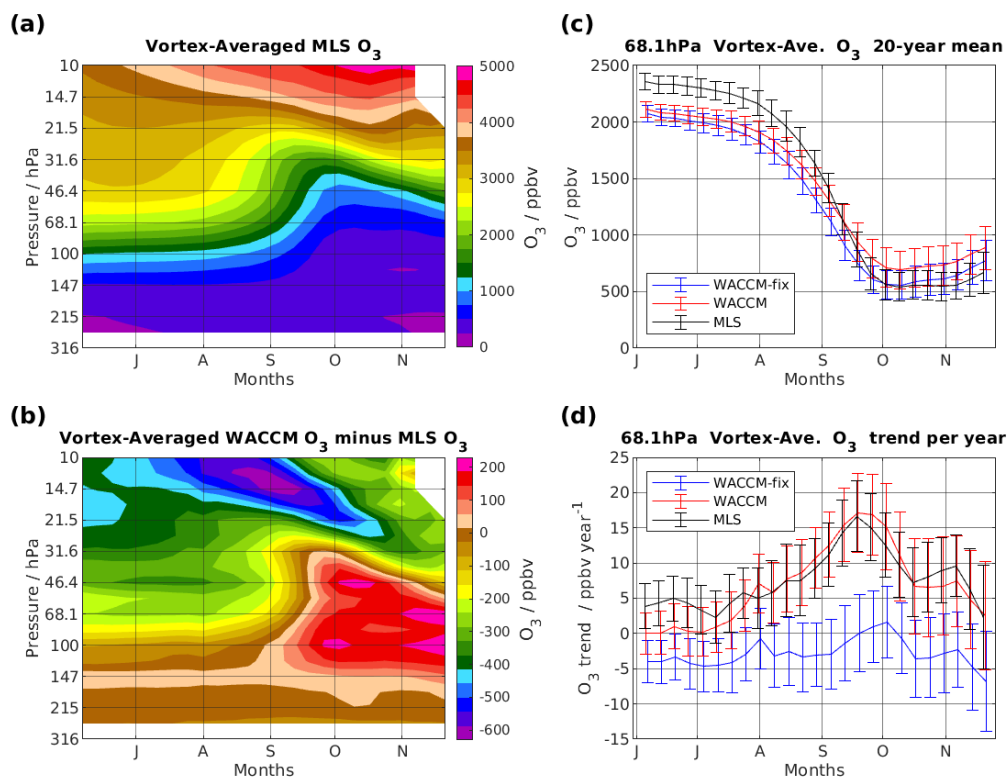


WACCM Vortex O₃ minus July 1-10 baseline



957
958
959
960

Figure 2. Same as Fig. 1, but for the WACCM simulation and without year 2024.

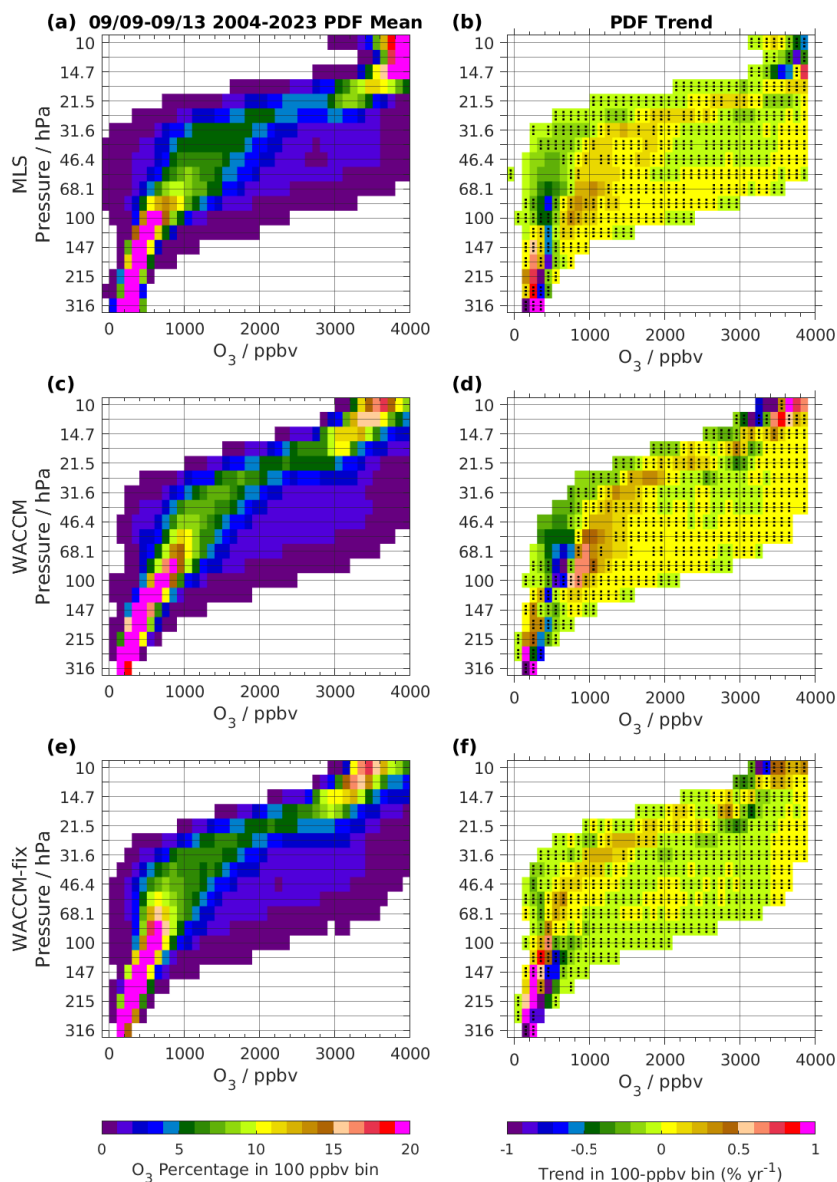


961

962 **Figure 3.** (a) Weekly mean Antarctic vortex-average ozone values from MLS in the lower
 963 stratosphere from early June to late November (weeks centered on day of year 157–325) for 2004
 964 through 2023. (b) Average values from WACCM, as in (a), minus the MLS values shown in (a).
 965 (c) Example at 68 hPa of the mean ozone abundances for 2004–2023 from MLS, WACCM, and
 966 WACCM-fix-EESC (labelled “WACCM-fix”); the error bars represent the interannual standard
 967 deviation about the mean in these weekly average values over all the years. (d) Ozone trends (ppbv
 968 yr⁻¹) at 68 hPa obtained by fitting a simple linear trend to the yearly O₃ values contributing to each
 969 weekly average. Weeks prior to the start of MLS science data collection on July 28, 2004 are not
 970 included in these averages; thus results for the first eight weeks are 19-yr averages and trends.

971

972



973

974

975

976

977

978

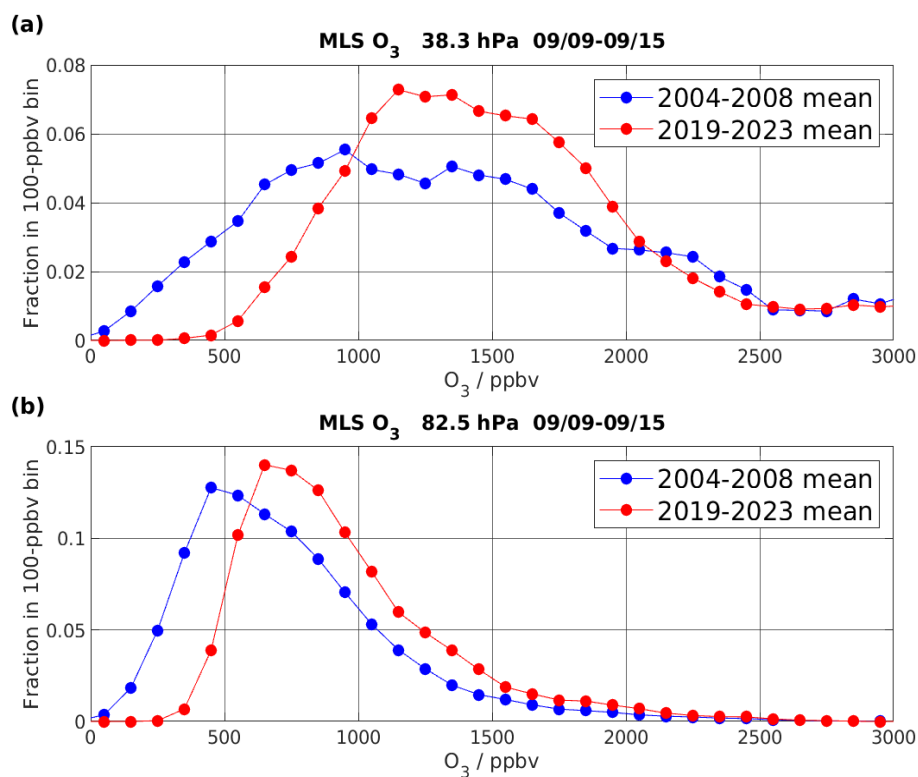
979

980

Figure 4. (a) Mean PDF for all years (2004 to 2023) during the week of September 9–15 (the week centered on September 12). (b) Trends in the population of the MLS PDF in (a) for a given level and mixing-ratio bin. Bins without black stippling have trends that are larger in magnitude than the 1σ uncertainty in the trend. (c) and (d) are the same as (a) and (b), respectively, but for the WACCM simulation. (e) and (f) are the same as (a) and (b), respectively, but for the WACCM-fix-EESC simulation.



981
982
983
984
985
986

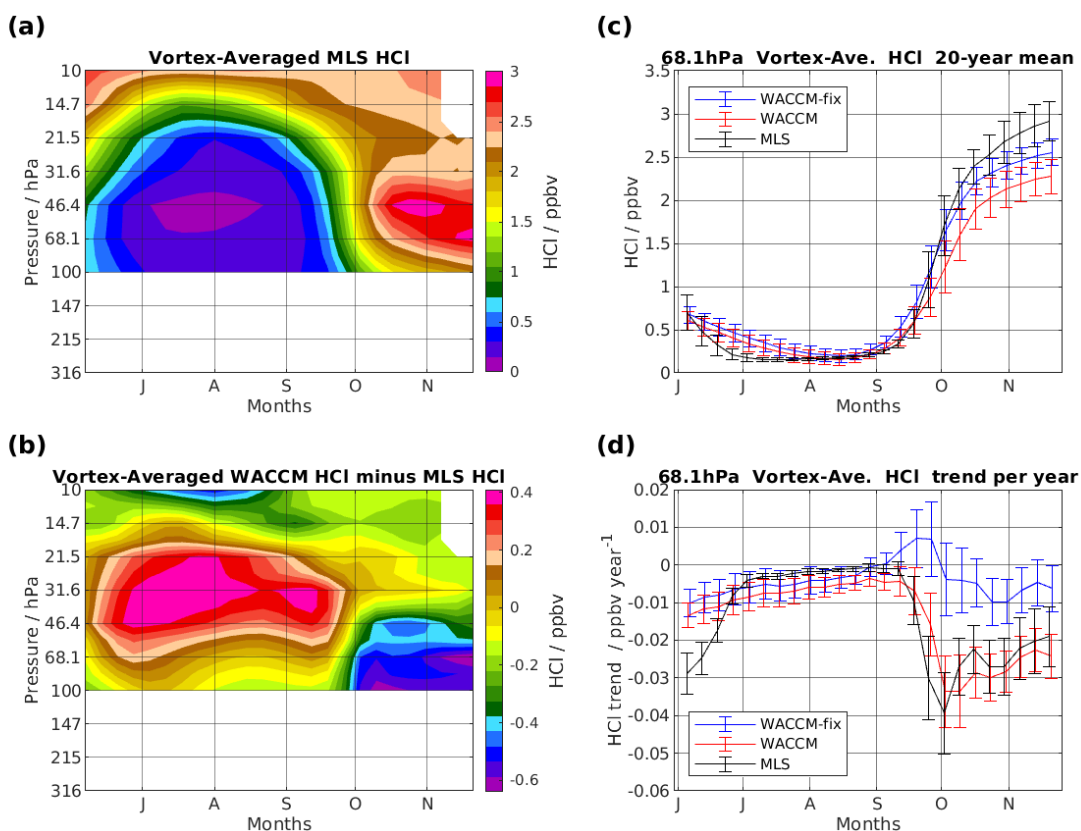


987
988
989
990
991
992
993
994
995
996
997
998
999
1000
1001
1002

Figure 5. Fraction of the Antarctic vortex-average MLS ozone distributions in each 100 ppbv bin, for the week centered on September 12 for the periods 2004–2008 (blue) and 2019–2023 (red), at (a) 38.3 hPa and (b) 82.5 hPa.



1003
1004
1005
1006
1007
1008

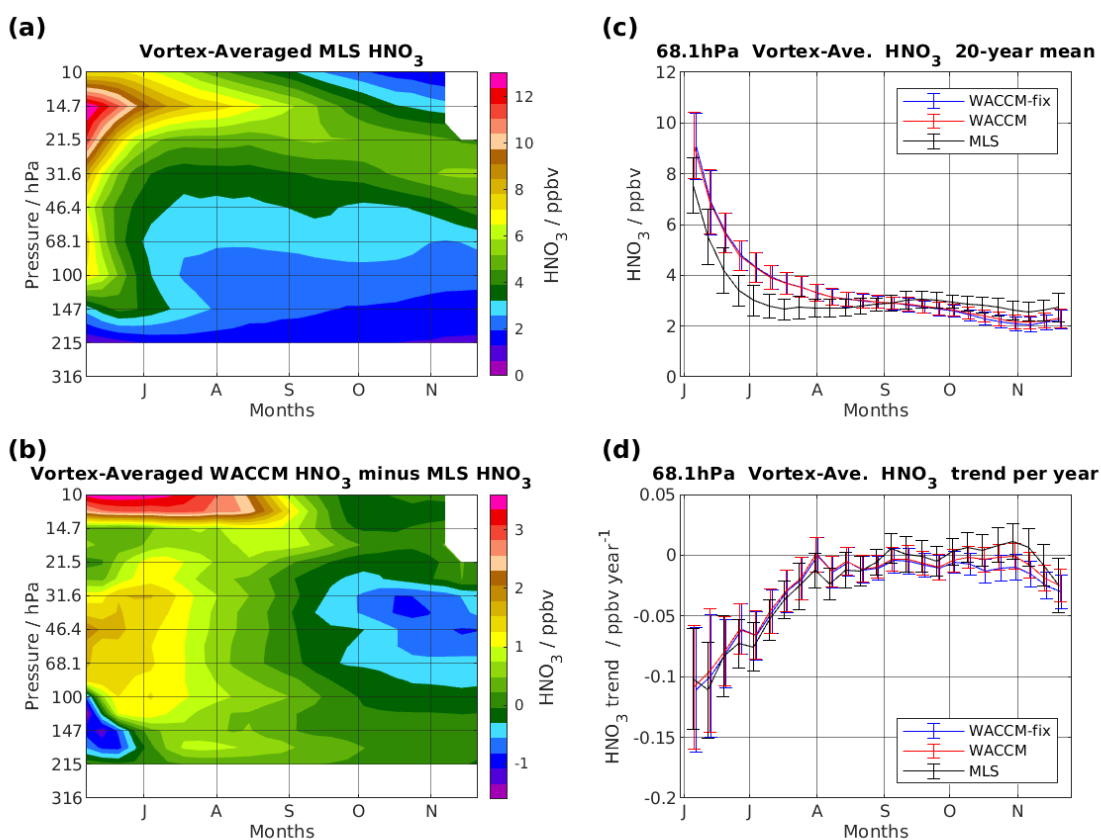


1009
1010
1011
1012
1013
1014
1015
1016
1017
1018
1019
1020
1021
1022

Figure 6. Same as Fig. 3, but for HCl.



1023
1024
1025
1026
1027
1028
1029

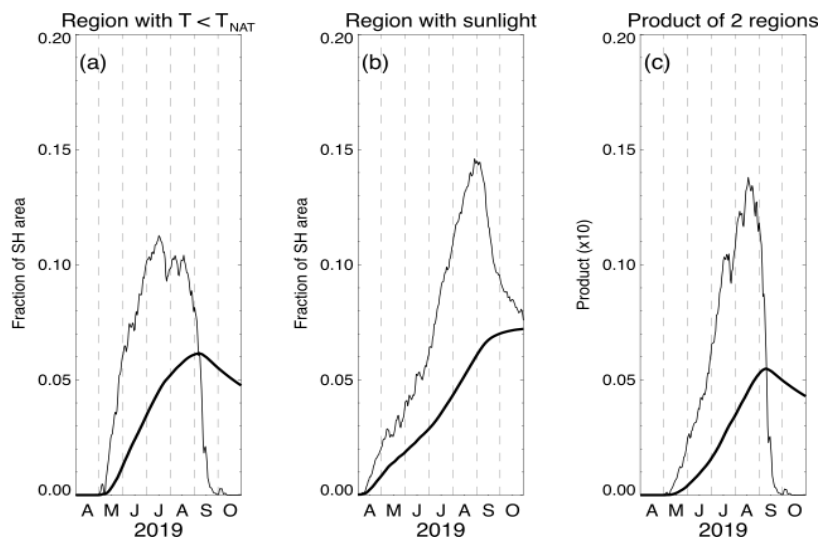


1030
1031
1032
1033
1034

Figure 7. Same as Fig. 3, but for HNO₃.

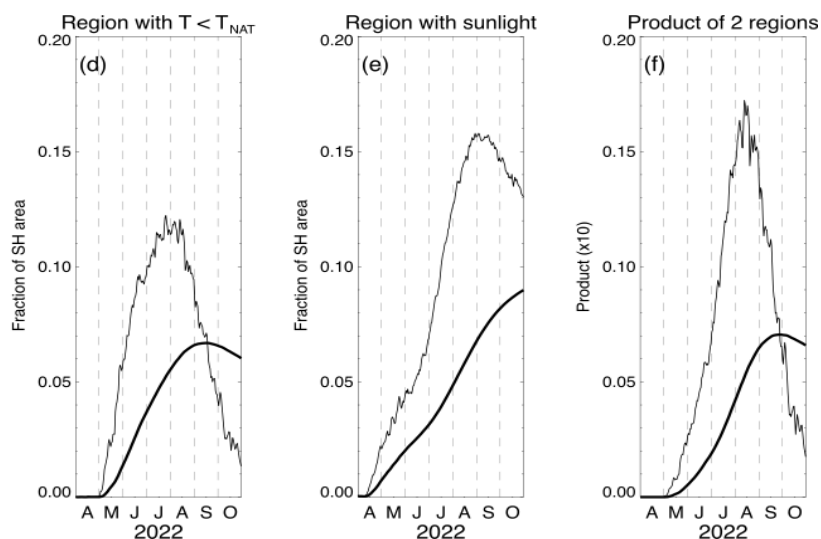


1035



1036

1037



1038

1039

1040

1041

1042

1043

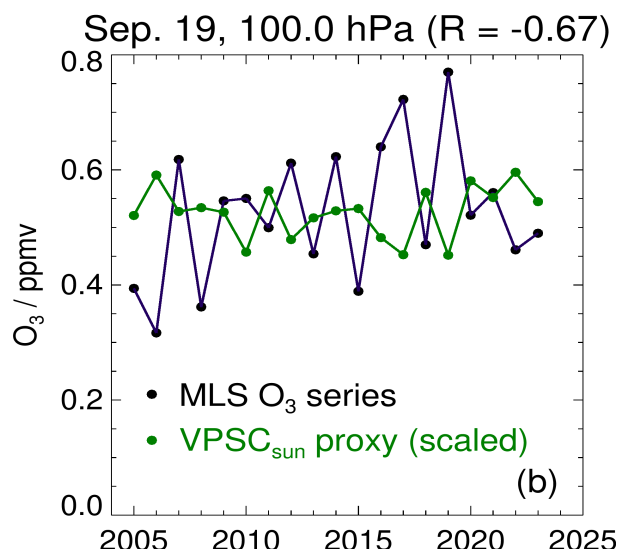
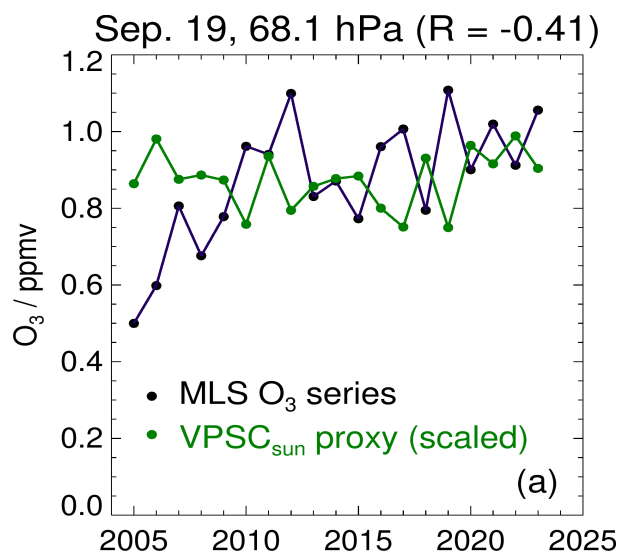
1044

1045

1046

1047

Figure 8. The lower stratospheric layer-average Antarctic vortex area with $T < T_{NAT}$ for (a) 2019 and (d) 2022; the lower stratospheric layer-average Antarctic vortex area exposed to sunlight for (b) 2019 and (e) 2022; and the product (multiplied by 10) of these two layer-average areas for (c) 2019 and (f) 2022. Layer averages are calculated over potential temperature levels from 330 K to 620 K. The thin lines depict daily quantities, whereas the thick lines are cumulative values of these quantities through each day of the year, from April 1 to October 31. The layer-average area diagnostics are expressed as a percentage of the total Southern Hemisphere (SH) area.

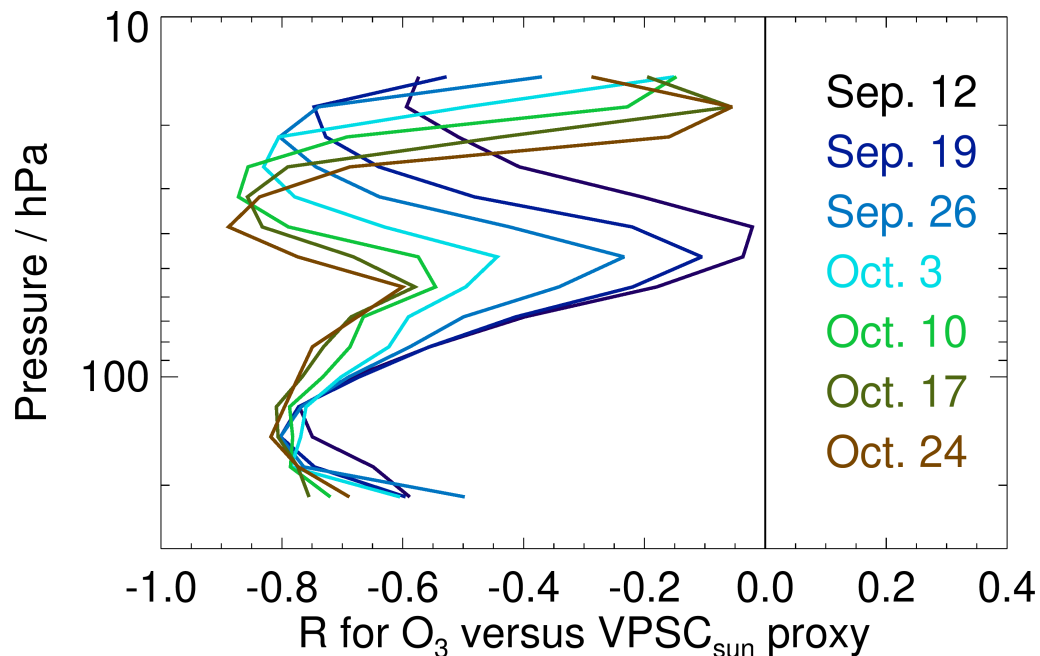


1048
1049
1050
1051
1052
1053
1054
1055
1056
1057
1058

Figure 9. Vortex-average Antarctic ozone variations from MLS (black) over 2005–2023 for the week centered on September 19 at (a) 68 hPa and (b) 100 hPa. The green lines are a scaled version of the variability in the $VPSC_{sun}$ proxy term described in the text (in relation to Fig. 8).

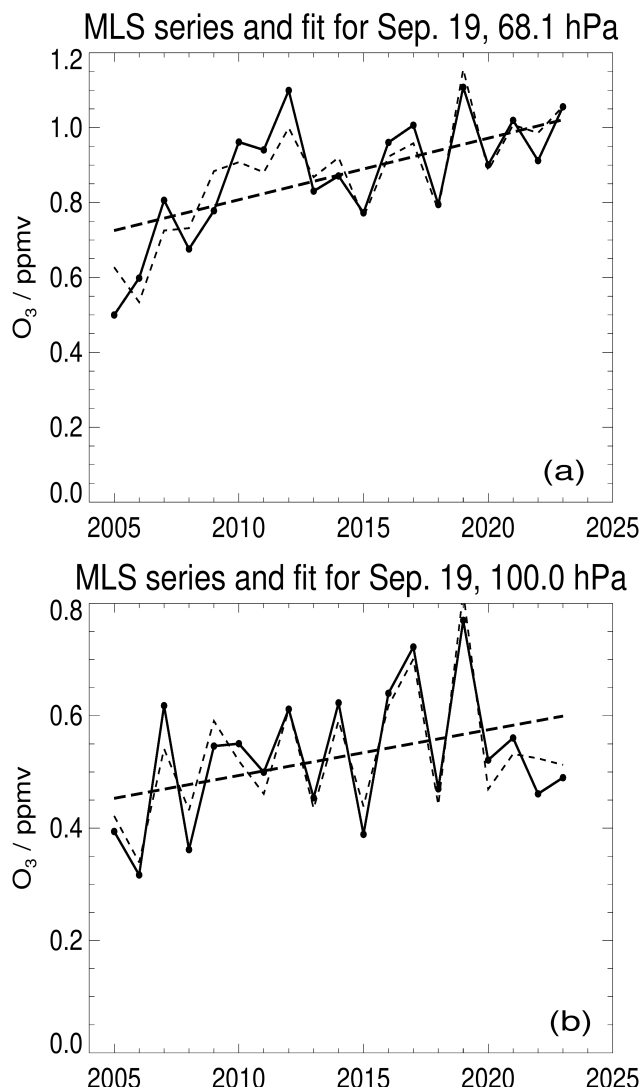


1059
1060
1061



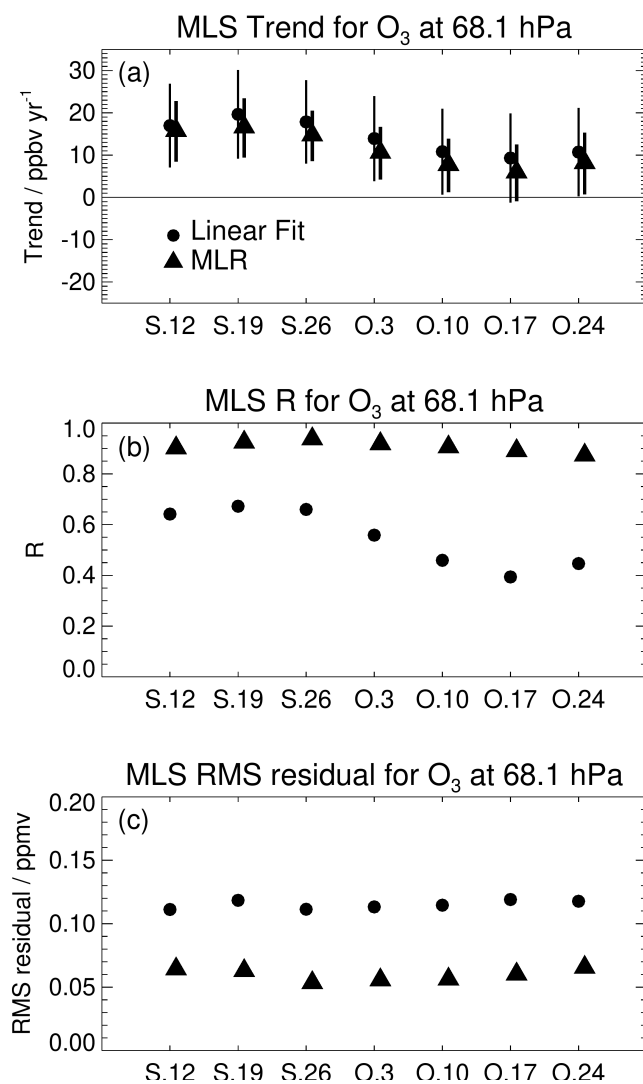
1062
1063
1064
1065
1066
1067
1068
1069
1070
1071
1072

Figure 10. An expanded view of the correlation coefficient (R) between the ozone vortex-average time series and the lower stratospheric $VPSC_{sun}$ proxy described in the text and in Fig. 8. Results are shown as a function of pressure for each of the September and October weeks considered here, as labeled on the right side of this plot.



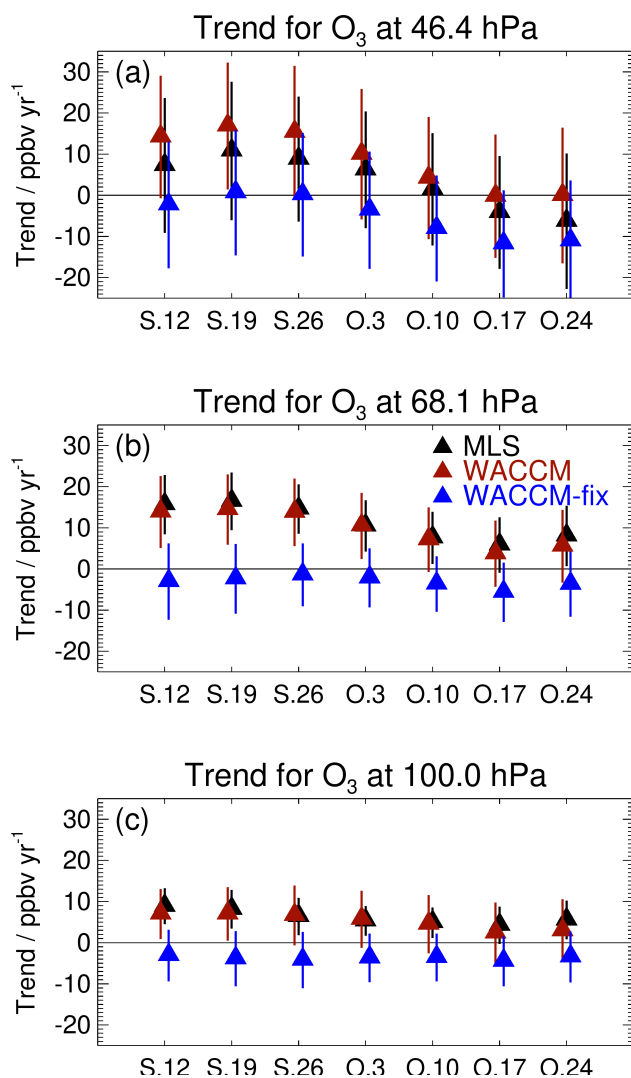
1073
1074
1075
1076
1077
1078
1079
1080

Figure 11. Examples of MLR fits to the MLS vortex-average ozone time series at (a) 68 hPa and (b) 100 hPa for the week centered on September 19. The MLS ozone averages are given by the solid line, the ozone trend (slope component of the MLR fit) is shown by the thick dashed line, and the thin dashed line gives the full fit from the MLR analysis.



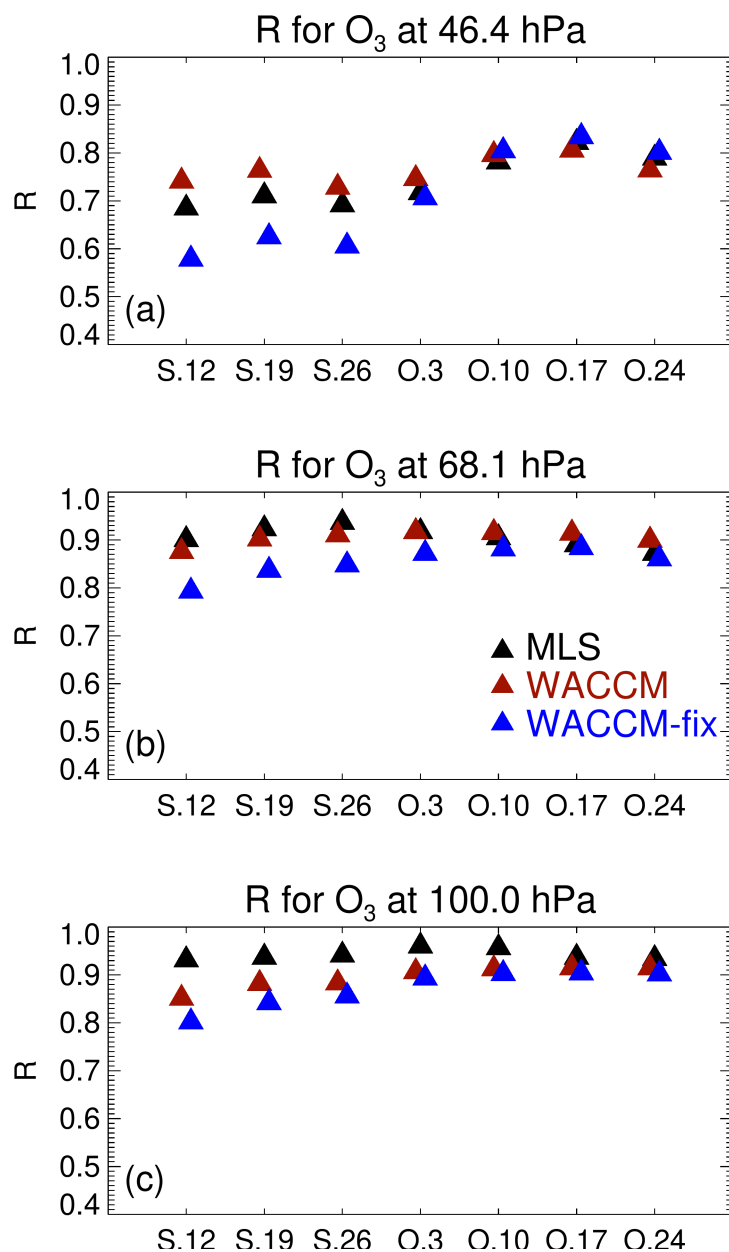
1081
1082
1083
1084
1085
1086
1087
1088
1089

Figure 12. Results at 68 hPa for (a) the trends in MLS vortex-average ozone over Antarctica, (b) the correlation coefficients between the fits and the MLS O₃ series and (c) the RMS residuals for these fits, as a function of weeks in September and October (centered on September 12, labeled S.12, to October 24, labeled O.24). The filled circles and filled triangles represent results from a simple linear fit and MLR, respectively, for 2005–2023. Trend error bars in (a) represent 2σ.



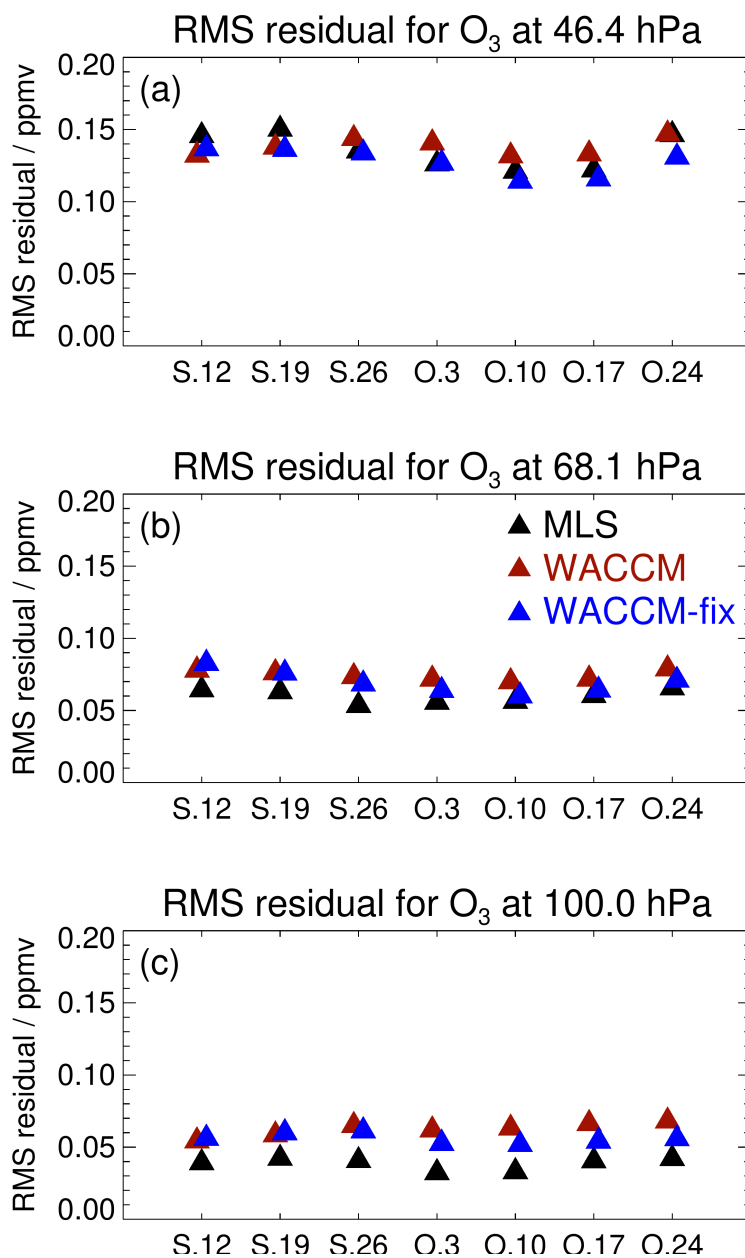
1090
1091
1092
1093
1094
1095
1096
1097
1098
1099
1100
1101

Figure 13. A comparison of the vortex-average trends for 2005–2023 based on MLR analyses from MLS, WACCM, and WACCM-fix-EESC (labeled WACCM-fix) for the weeks from September 12 through October 24 for (a) 46 hPa, (b) 68 hPa, and (c) 100 hPa.



1102
1103
1104
1105
1106
1107
1108
1109

Figure 14. Same as Fig. 13, but for the correlation coefficients (R) calculated for the MLR fits to the vortex-average ozone time series.



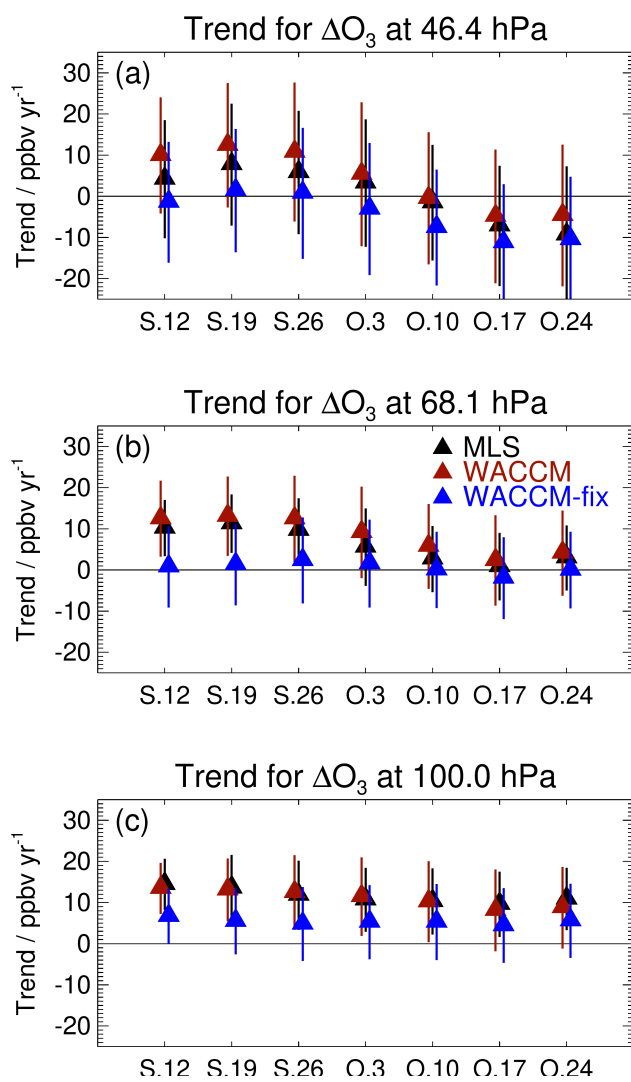
1110
1111
1112
1113
1114
1115

Figure 15. Same as Fig. 13, but for the RMS residuals of the MLR fits to the vortex-average ozone time series.



1116

1117



1118

1119

1120

1121 **Figure 16.** Same as Fig. 13, but for MLR analysis results from time series of vortex-average ozone

1122 in the first week of July subtracted from the September and October weekly average ozone values;

1123 we refer to this methodology as ΔO_3 analyses rather than O_3 analyses.

1124

1125

1126

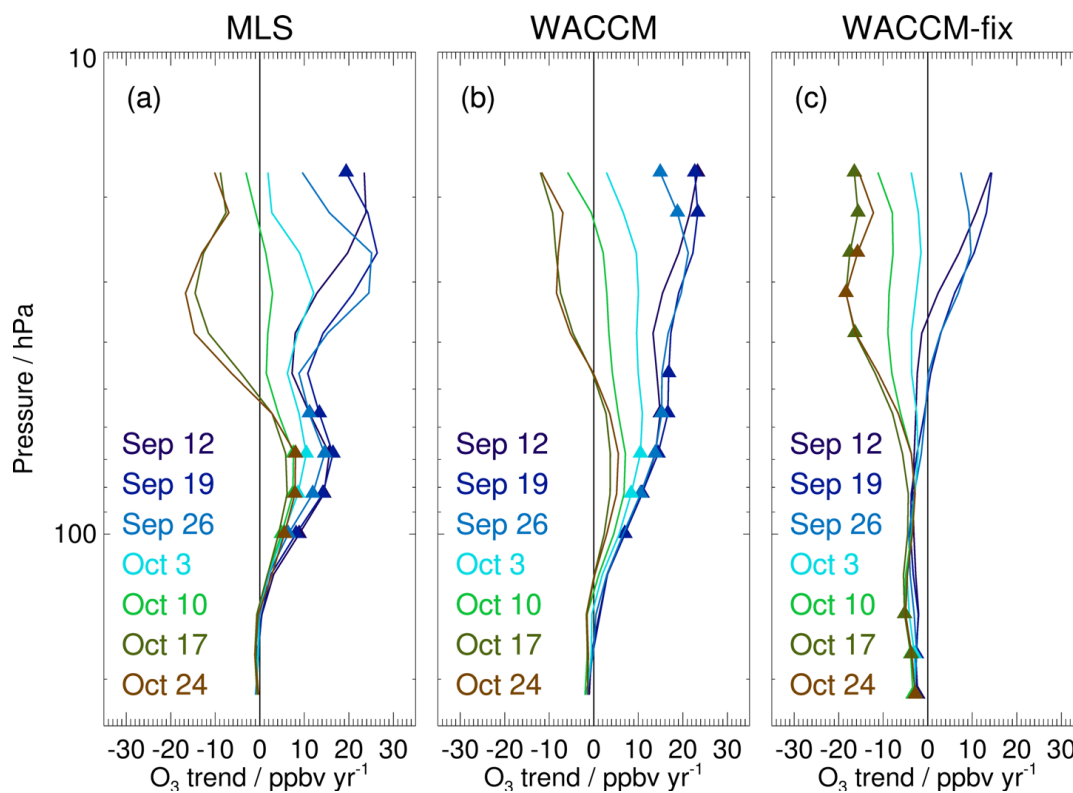
1127

1128

1129



1130
1131
1132
1133

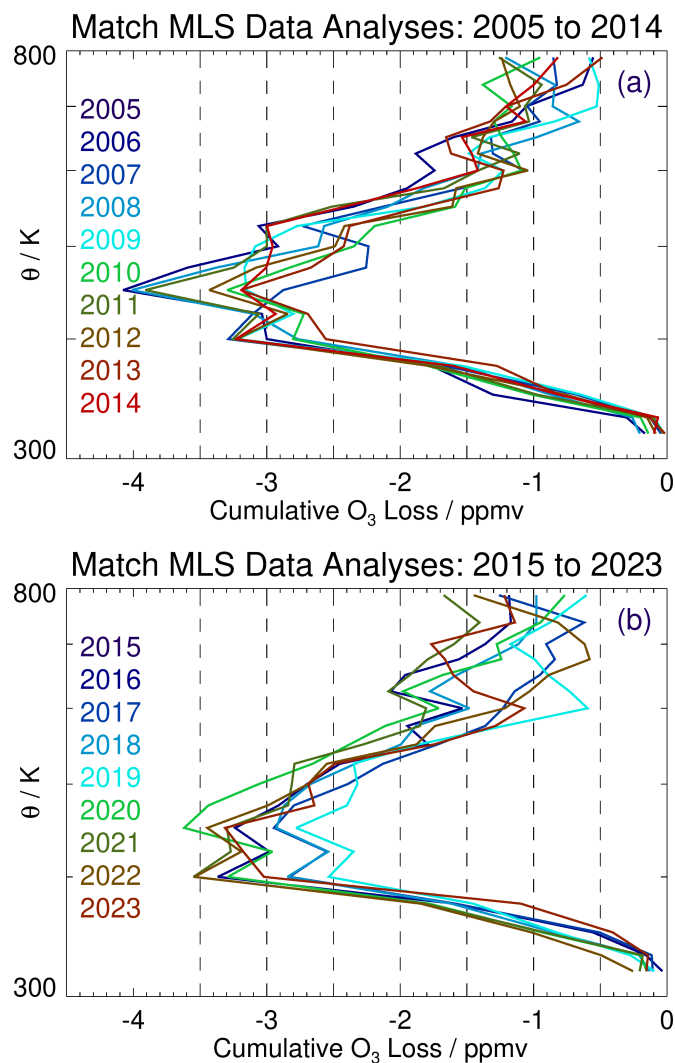


1134
1135
1136
1137
1138
1139
1140
1141

Figure 17. Trends in Antarctic vortex-average ozone from (a) MLS, (b) WACCM, and (c) WACCM-fix-EESC (labeled WACCM-fix) based on MLR analyses from 2005 to 2023. The different curves depict weekly averages centered on the dates shown. The trends that exhibit statistical significance at the 2σ level are marked by triangles.



1142



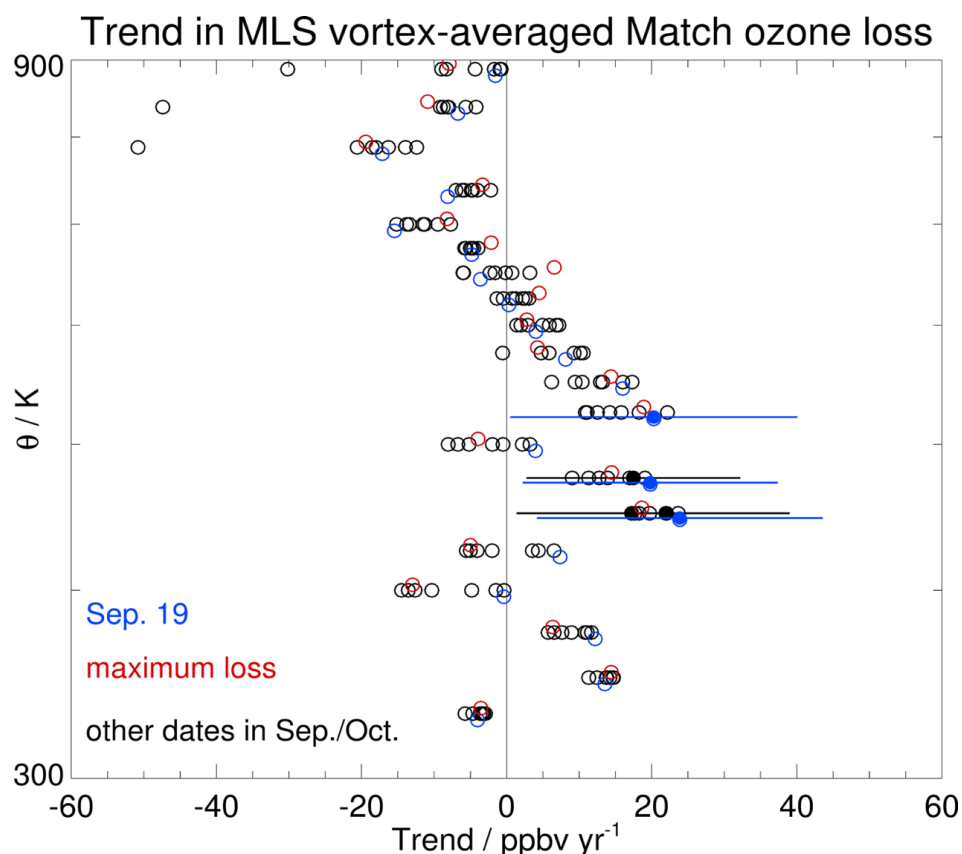
1143

1144

1145 **Figure 18.** Profiles of maximum cumulative ozone losses from the Match technique inside the

1146 Antarctic vortex, based on weekly averages in the winter/spring for (a) 2005–2014 and (b) 2015–

1147 2023.



1148

1149

1150

1151 **Figure 19.** Chemical ozone loss trend profiles inside the Antarctic lower stratospheric vortex from

1152 Match-based analyses of MLS data from May through October, for 2005–2023. Only a few trends,

1153 marked by the filled circles with associated (2σ) error bars, are significant; for clarity, other error

1154 bars are omitted. The blue circles are for the week centered on September 19, the red circles are

1155 trends based on the maximum cumulative losses for each year, and the other points (in black)

1156 represent trend values for the other analyzed weeks, from September 12 to October 24.

1157

1158